UNIVERSITÀ
degli STUDI
di CATANIA

Dipartimento
di Fisica
e Astronomia
"Ettore Majorana"

PhD programme in Material Science and Nanotechnology

Mattia Pizzone

Innovative strategies for the conformal doping of semiconductors

PhD thesis

Supervisors:
Chiar.ma Prof. M. G. Grimaldi
Dr. R. A. Puglisi

academic year 2022/2023

Contents

Introduction

In this day and age, the technology landscape is undoubtedly dominated by semiconductors and semiconductor devices. Their history starts in the early-to-mid-1800s, with the discovery of an "extraordinary case" of electrical conduction by Michael Faraday, who observed the increase of electrical conduction with temperature in silver sulfide crystals [1]. This was unexpected, since the opposite can be observed in metals like copper and pure silver. Although these materials were initially classified as "bad conductors" or "strange conductors", they caught the interest of the scientific community. After a century of studies, the first formal theory about them was published, called "The theory of electronic semi-conductors" [2] by Alan Wilson in 1931, which explains the observed phenomena in terms of quantum mechanics. This enabled subsequent scientists to exploit these systems critically. As a matter of fact, after the introduction of this theory, many discoveries and inventions were made, including but not limited to the semiconductor diodes [3] (Russel Ohls, 1940), the junction transistor [4] (William Shockley, 1948), the first all-semiconductor circuit [5] (Jack Kilby, 1958), the tunnel diode [6] (Leo Esaki, 1958). In the following years, these technologies became essential in the fabrication of miniaturized electronic devices and were used to make microprocessors, ROMs, RAMs and computer chips. The downscaling of the electronic components became, itself, object of study. This prompted Gordon Moore first and then Robert Dennard to give birth to the Moore's law [7] and give it a scientific foundation [8], respectively. While Moore understood that the number of components per chip would double every 12 months (figure

1a), thus enhancing their performance, Dennard noticed that the horizontal dimensions of a transistor and the speed of the devices would scale by the same factor (figure 1b).

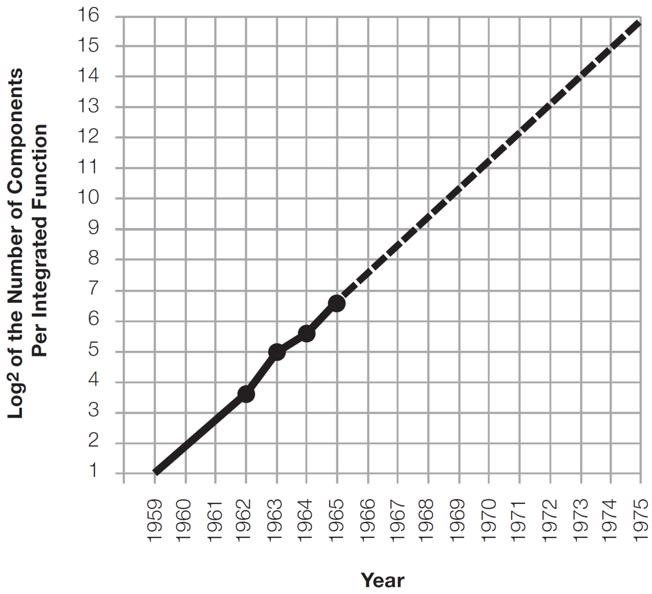

(a)

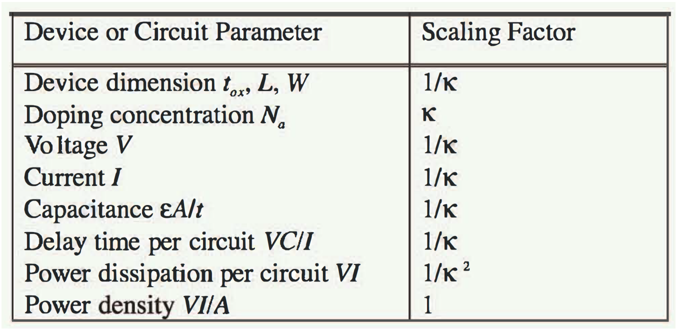

Device or Circuit Parameter	Scaling Factor
Device dimension t_{ox}, L, W	$1/\kappa$
Doping concentration N_a	κ
Voltage V	$1/\kappa$
Current I	$1/\kappa$
Capacitance $\varepsilon A/t$	$1/\kappa$
Delay time per circuit VC/I	$1/\kappa$
Power dissipation per circuit VI	$1/\kappa^2$
Power density VI/A	1

(b)

Figure 1: *(a) Number of components per integrated function vs years as per Gordon Moore's law [7]; (b) Robert Dennard's results: as the device dimension shrinks by a factor of k, the same factor is applied to other parameters [8]*

Although Moore's law was born with the purpose of describing the relation between component downscaling and device performances over time, it quickly transformed into a roadmap for the industry to follow: by abiding to this new, auto-imposed schedule, companies could predict the future performances of electronic devices and design their own technologies accordingly. As a matter of fact, complying with the Moore's law wasn't strictly related to competition, but also gave the whole industry - especially the computer science and information technology related ones - a steady pace of progress. This highlighted the importance of founding these everchanging technology on an abundant, easy-to-manufacture semiconductor with the necessary electrical and morphological properties. Silicon, with its high purity, robust electrical properties engineering and, most of all, natural abundance, became the perfect candidate for mass production and technology advancements, and has enabled the scientific community and the industry to reach their current maturity.

The key feature that enabled semiconductors to be widely spread is the possibility of modifying the semiconductor local electrical properties with a process called "doping", which is the act of artificially and controllably introducing particular atomic impurities that provide the material with charge carriers. By doping adjacent areas of the same semiconductor sample and assembling building blocks of different materials, it is possible to design and fabricate devices: solar cells, light emitting diodes (LEDs), photodetectors and, most of all, metal oxide semiconductor field effect transistors (MOSFETs). These devices are the main constituents of current technology and are, mostly, bidimensional objects. These can be as small as the building technology permits. While in the 1970s these devices were 10 µm wide [9], the current technology allows for the production of 5 to 10 nm sized MOSFETs [10, 11]. As the dimension of these components approaches the single nanometer, an obvious question arises: is the era of the Moore's law coming to an end? As a matter of fact, the general opinion skews towards the necessity of abandoning the "law of shrinking" in favor of new 3D, nanostructure-based technologies - like finFETs for the 5 nm FET technology - that will exploit the unique structural and electrical properties of nanometer-sized objects [12] and could enable the industry to set aside the Moore's law and evolve into a new dimension. This Ph.D. thesis is focused on the investigation of some aspects of the Molecular Doping (MD) technique, introduced in 2008 by J.C. Ho et al. [13] as an innovative conformal doping technique, as well as the application of it to SiC substrates.

In chapter 1, the general aspects of semiconductor properties and doping are recalled. A brief introduction on the process of doping and current widespread doping techniques is presented.

In chapter 2, the literature on MD and its possible applications is summarized and explained. After the presentation of the technique, the aspects about the tuning of electrical properties of doped samples are treated together some applications to micro- and nano- structured systems.

In chapter 3, elements of the nucleation theory are explained. These are fundamental in order to understand the experimental work of this thesis. The nucleation and growth thermodynamics is introduced and the Avrami equation is demonstrated.

In chapter 4, the evaluation of nucleation and growth during the MD molecule deposition step is performed both morphologically and with computational methods, with a focus on the bond nature between the precursor molecule and the substrate, together with the evaluation of the final electrical properties of doped samples.

In chapter 5, the study of the influence of molecule deposition parameters on final electrical properties of the samples is presented. Through the comparison between electrical and morphological data, several aspects of the molecular layer formation are highlighted.

In chapter 6, the possibility of applying the MD process to SiC substrate is explored through the study of preliminary samples. The behaviour of Ni layers in the MD process is evaluated and some investigations proposed.

Finally, the results of this thesis are summarized in the conclusions, together with the discussion of possible approaches in the understanding of some unclear aspects of the experimental work presented so far.

Chapter 1

Semiconductors and doping

1.1 Doping

Understanding why semiconductors are such a great resource for modern electronics requires a dive into the physics of the conduction in these materials. The term "semiconductor" refers to a class of materials with a unique conductive behaviour, associated with their electronic band structure. These "bands" are formed by the interaction of quantum states for electrons and, in order to observe charge transport, electrons must occupy partially filled, delocalized states. A high conductivity material is characterized by the presence of many partially filled electronic states, while an insulator has very few. Two main bands, formed by bundles of electronic states, can be recognized in the electronic structure: the "valence band" and the "conduction band". These bundles of electronic states are separated by a "gap", energywise, and the extent of this gap is used as a reference to roughly classify materials into three groups: insulators, semiconductors, and metals. Although it's not a hard classification, wide band gap materials (> 4 eV) are considered insulators, while semiconductors are characterized by a smaller energy gap (< 4 eV). Table 1.1 shows the band gap associated with widely used semiconductors. In contrast, metals are characterized, respectively, by the contact and the overlap of the energy bands. A simple schematic can be found in figure 1.1.

Undoped semiconductors are called "intrinsic" while doped semicon-

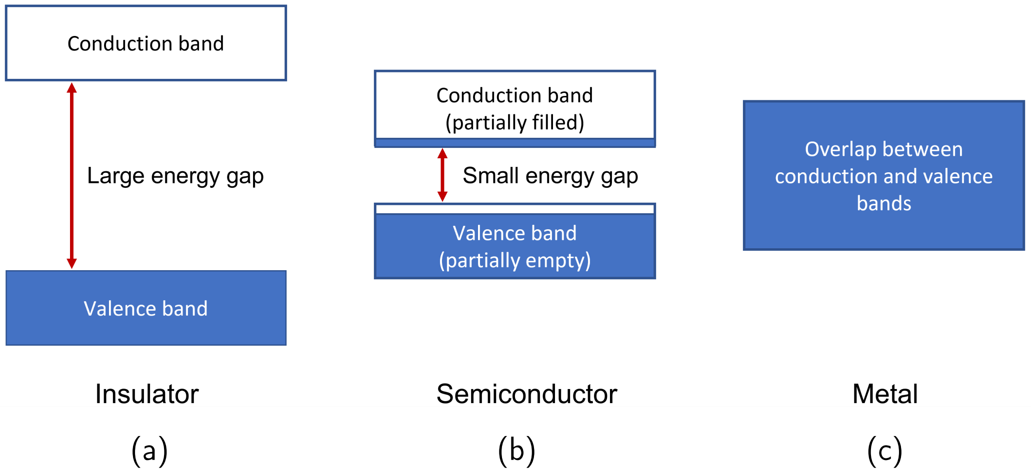

Figure 1.1: *Schematics of valence and conduction band of materials. (a) Insulators have a wide bandgap, the conduction band is empty while the valence band is full; (b) Semiconductors have a small semiconductors and electrons can jump between bands more easily; (c) Metals do not have an energy gap, there's an overlap between electron bands.*

Name	**Symbol**	**E_g (eV)**
Silicon	Si	1.12
Germanium	Ge	0.66
Gallium Arsenide	GaAs	1.43
Gallium Nitride	GaN	3.4
Indium Phosphide	InP	1.35

Table 1.1: *Widely used semiconductor energy gaps. Data taken from [14].*

ductor are called “extrinsic”. The mechanism taking part into semiconductor doping involves the substitution of a native atom with different elements: for example, silicon - a group IV element in the periodic table - is usually doped with group III and V elements, which will provide, respectively, positive and negative charge carriers. In bulk silicon, each valence electron will bind to other neighbour atoms’ valence electrons. By adding an atom with three or five valence electrons into the lattice, a "hole" or an extra, weakly-bound electron is also introduced into the semiconductor. An atom that, when introduced into a lattice, provides electrons is called "donor", while one that provides holes is called "acceptor". A schematic of the process can be found in figure 1.2.

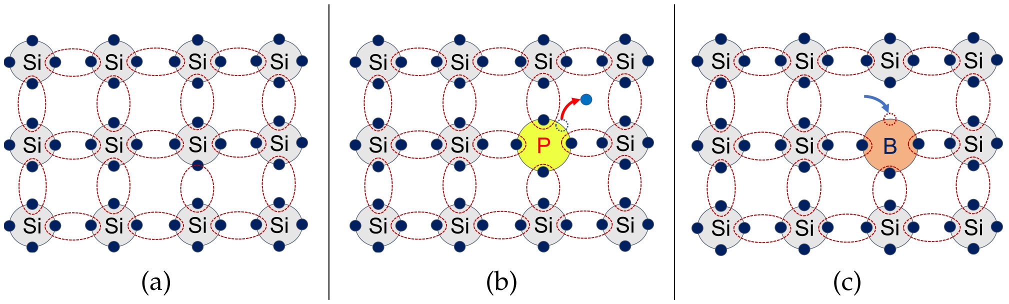

(a) (b) (c)

Figure 1.2: *Silicon lattice schematics: (a) intrinsic lattice, (b) n-type lattice doped with phosphorus, (c) p-type lattice doped with boron. While n-type doping provides the lattice with free electrons, p-type doping allows charge carriers to move by removing electrons, leaving a "hole".*

The act of doping typically modifies their electrical conductivity by a factor of several thousands. For example, 1 cm^3 of metal contains 10^{22} free electrons, while the same volume of Silicon at 20 °C contains carriers by the order of 10^{10} [15]: the addition of 0.001 % of phosphorus (an electrically active impurity of silicon) introduces about 10^{17} electrons, which increases the electrical conductivity of the material accordingly. It must be said that, in order for this to happen, the doping atoms must occupy a "substitutional" spot in the semiconductor lattice - i.e. a position in the crystal that is normally occupied by a native atom - otherwise it won't be electrically active. Doping can be achieved in several ways with a plethora of techniques, the most widespread of which will be presented in the next paragraphs.

1.2 Doping methods

In this section, some of the most used doping techniques will be described and their main strengths and issues will be briefly highlighted, in order to have a frame of reference of the current landscape on doping methods.

Ion implantation, Epitaxial doping and Diffusion based methods will be presented.

1.2.1 Ion implantation

Ion implantation is the act of driving impurities into a substrate by accelerating ionized impurity atoms towards its surface. It finds applications in metal surface finishing, nanoparticle formation and the doping of semiconductors. Its setup, shown in figure 1.3, typically consists in an ion source, where the species to be implanted are ionized, an ion accelerator, where ions are accelerated, collimated and directed through the use of electromagnetic fields and a target chamber where the material to be implanted is set. The whole process is performed in vacuum.

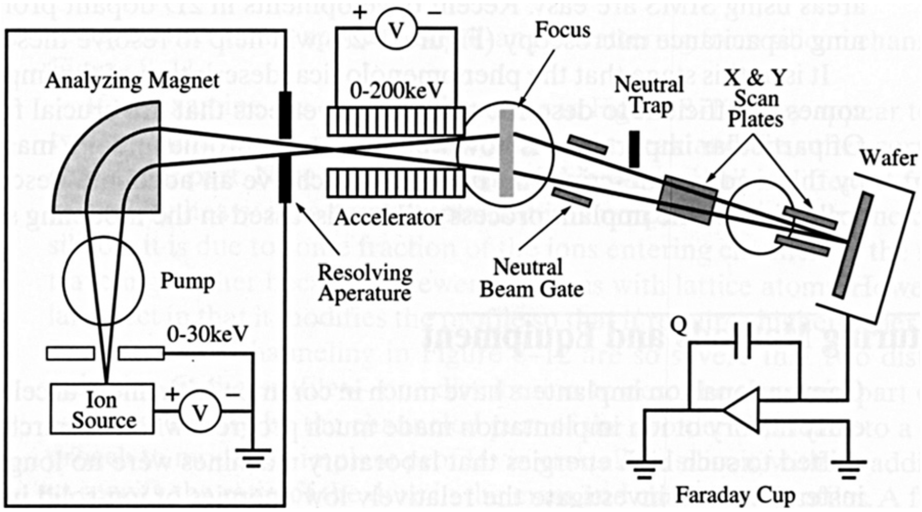

Figure 1.3: *Ion implantation set up [16].*

In addition to the fundamental components, implanters usually have some functional components like current integrators (to calculate the implanted dose), mass and charge selectors for ions - usually consisting in electric and magnetic fields that can separate particles with specific mass-charge ratios - and slits, which allow only particular species to reach the target and block the rest. A thermal process is necessary to let the implanted impurity become electrically active. Although it is vastly used in semiconductor industry, ion implantation presents various issues, like:

- *Damage and recovery*: to be implanted, ions have to penetrate the surface of the samples. This inevitably introduces defects like point defects and dislocations in the lattice. These can be responsible for device failure or leakage currents. Thermal processes usually - but not always - regenerate the damage. This is especially important for nanostructures, which can be heavily modified by the process;

- *Amorphization*: since ions force their way to the aimed depth, they usually modify the periodicity of the lattice they enter. Enough modifications lead to amorphization, i.e. a complete loss of periodicity, that changes electrical and optical properties of the interested areas;

- *Sputtering*: the ion-surface impacts can slowly etch the sample surface by ejecting its atoms. In addition, ejected atoms can also deposit on other areas of the sample, where they could act as unwanted defects.

1.2.2 Epitaxial doping

Epitaxy (from *epi* meaning "upon" and *taxis* meaning "ordered") is a term indicating the growth of thin crystalline layers on a crystalline substrate. The substrate is used as a "seed" onto which deposited atoms can adjust, to follow its crystal lattice orientations. While "Homoepitaxy" refers to the growth of crystalline layers of the same species as the seed substrate, "heteroepitaxy" is a kind of epitaxy performed between different materials. By introducing doping impurities along with the material to be deposited, doped layers can be grown. Chemical Vapor Deposition (CVD) and Molecular Beam Epitaxy (MBE) are two of the most used set-ups for epitaxial growth:

- *Chemical Vapor Deposition*: A form of epitaxial growth characterized by the use of molecules that, by reacting with the substrate surface, release the atom to be deposited. A simplified set up is shown in figure 1.4. It is used to create atom layers on a substrate and the doping is achieved by introducing dopant precursors alongside other precursors species.

The process, which requires an ultra-high vacuum, involves the introduction of the reactant into the substrate chamber, its adsorption on the substrate surface, the release of the atom to be deposited. The residual reactants and byproducts have to be removed from the chamber contin-

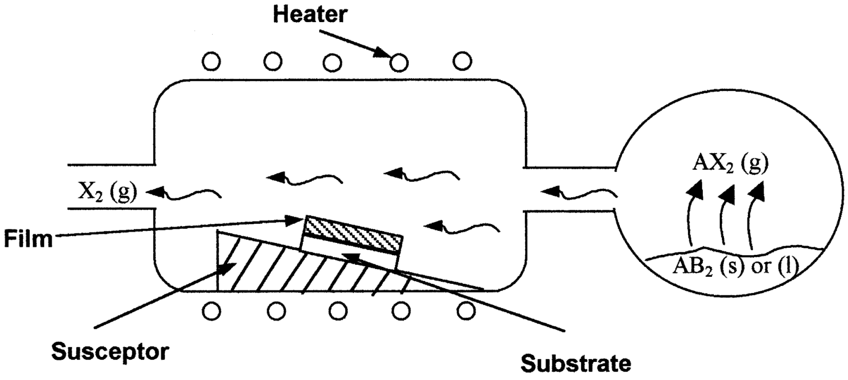

Figure 1.4: *Schematics of a CVD chamber. The precursor molecules, here generalized as* AX_2*, get adsorbed on the sample surface and release the atoms to be deposited (species A). Byproducts, indicated as* X_2*, are either removed from the chamber or re-deposited on the sample, acting as defects. [17]*

uously for the process to be efficient. CVD allows for a high growth rate, but it is based on the use of potentially dangerous precursors in gas phase. In addition, residues of the surface chemical reaction could remain on the substrate and act as defects [17]. - *Molecular Beam Epitaxy*: MBE utilizes evaporation of the atomic species to be deposited and therefore doesn't involve chemical reactions between precursor species and the substrate surface. The setup is shown in figure 1.5.

In its essence, the process involves the evaporation of atoms from solid phase, vaporized inside heat-resistant containers called effusion cells, and deposited on the substrate kept at high temperature, typically between 400°C and 800°C. The growth rate is monitored through in-situ systems like Quartz-Crystal Microbalance (QCM) and Reflection High-Energy Electron Diffraction (RHEED), making the technique very precise in this regard. Although the technique allows for a precise control of layer growing and doping, it involves the use of very expensive equipment and needs to be heavily maintained [18].

Regardless of the set-up, epitaxial doping incurs in two main issues: outdiffusion and autodoping. The high temperatures at which the substrates have to be kept in order for the techniques to achieve the desired

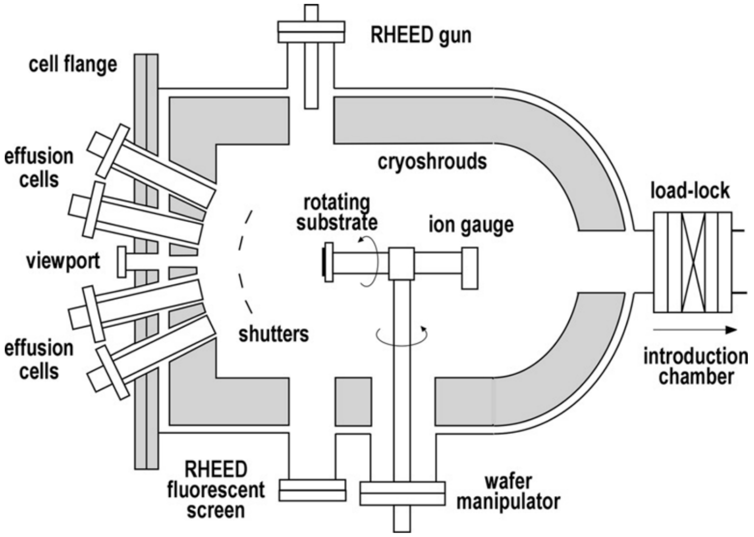

Figure 1.5: *Representation of a MBE set up. Species to be deposited are stored into effusion cells, they are vaporized and allowed to reach the substrate as "beams". Shutters may be used to interrupt the flow. The RHEED monitoring lets the user recognize the formation of complete layers [18].*

result allow for the inter-mixing of doping impurities between different grown layers (outdiffusion) and the penetration of dopant impurities from the epitaxial layer into the substrate and vice-versa (autodoping). Both of these phenomena modify the electrical properties of the substrates in an unwanted fashion.

1.2.3 Diffusion based methods

These methods are all based on the phenomenon of diffusion, i.e. the net transport of atoms from a region of higher concentration to a region of lower concentration. The result is a gradual mixing of materials. In semiconductors, this is usually achieved by raising the sample temperature after creating an impurity concentration imbalance between the surface and the bulk of the sample. The diffusion phenomenon is mostly delineated by the unidimensional first and second Fick's laws, which describe the flux of the diffusing atoms with the expressions:

$$F = -D\frac{\delta C}{\delta x} \tag{1.1}$$

$$\frac{\delta C(x,t)}{\delta t} = D\frac{\delta^2 C}{\delta x^2} \tag{1.2}$$

where F is the atoms flux, D is the diffusion coefficient, C (expressed in atoms/cm^3) is the concentration as a function of x, the depth of the surface and t, time. Moreover, the diffusion coefficient D is defined as:

$$D = D_0 exp(-\frac{E_a}{kT}) \tag{1.3}$$

where D_0 is a pre-exponential parameter, E_a is the activation energy of the process, k is the Boltzmann constant and T is temperature expressed in Kelvin. There are two most frequently used solutions for equations 1.1 and 1.2 depending on the boundary conditions: fixed surface concentration and fixed diffusing amount.

1. *Fixed surface concentration*: if the concentration of the impurity at the surface is kept constant, the boundary conditions can be expressed as $C(0,t) = const$ and $C(\infty,t) = 0$. In this case, the solution is given by:

$$C(x,t) = C_s erfc(\frac{x}{\sqrt{4Dt}}) \tag{1.4}$$

Where $erfc$ is the complementary error function (Appendix E). It is worth noting that, while $C(0,t)$ is considered constant, the total amount of incorporated dopant Q will be a function of time, as it is shown in the following equation:

$$Q(t) = \int_0^\infty C_s erfc(\frac{x}{\sqrt{4Dt}})dx = \frac{2\sqrt{Dt}}{\sqrt{\pi}}C_s \tag{1.5}$$

2. *Fixed diffusing amount* Q: in this case, the boundary conditions can be expressed as

$$\int_0^\infty C(x,t)dx = Q = const. \tag{1.6}$$

$$C(\infty,t) = 0 \tag{1.7}$$

The solution for such a system takes the form of a Gaussian function of depth x:

$$C(x,t) = \frac{Q}{\sqrt{\pi Dt}} exp(-\frac{x^2}{4Dt}) \tag{1.8}$$

As a consequence, the concentration at the surface can be expressed by the following:

$$C(0,t) = \frac{Q}{\sqrt{\pi Dt}} \tag{1.9}$$

This demonstrates that, with these boundary conditions, the dopant surface concentration tends to decrease as a function of time. This solution can be applied to doping techniques in which the impurity source is pre-deposited on the samples prior to the diffusion step and, since the dopant species is not replenished continuously during the process, $C(0,t)$ can't be considered constant. Regardless of the applied boundary conditions, the quantity $\sqrt{Dt}$ plays a fundamental role in the diffusion phenomenon and, with it, the parameters that govern the diffusion coefficient: the activation energy E_a and the temperature of the diffusion process T, as expressed by equation 1.3. An applicative example of the solution described in equation 1.4 is the diffusion from gas phase, in which a chamber is filled with a carrier gas (nitrogen, argon, etc.) that, enriched with the desired dopant in gaseus form (for example PH_3 or B_2H_6), is brought to the samples, onto which the concentration balance can take place. If, inside the chamber, the concentration of doping chemical species is kept constant, $C(0,t)$ can be considered constant, and this solution applies. An example technique in which equation 1.8 can be applied is the Spin On Dopant (SOD) method, which consists in the deposition of a uniform dopant-containing layer on the substrate using a spin coating method and the diffusion of the dopant through a subsequent thermal annealing.

1.3 Drawbacks of conventional methods

As it has been already mentioned, the semiconductor industry advancements have been based on the incremental scaling of device dimensions, in order to fit more into the same surface area, thus improving performances [19]. The main advantage into applying this principle is an economical one: this approach represents a sort of schedule that the industry can follow in order to invest in future products by having a prediction on how the future technology will be able to accomodate for it. However, even though the device scaling has been a steady process in the last five decades, a dramatic adjustment had to be made recently in order to maintain its linearity: the introduction of three dimensional geometries in semiconductor devices [20]. Among the most used doping techniques introduced in chapter one, none has been designed with the scope of nanostructure doping. Epitaxial doping and CVD methods fail to provide a conformal doping and are typically in-situ doping techniques, i.e. doping is achieved at the same time as the fabrication of the nanoarchitecture; ion implantation is instead an ex-situ doping technique but, as it is demonstrated in the work of R. Duffy et al. [21], it is especially unsuited for the conformal doping of high surface-to-volume ratio structures. The simulation is reported in figure 1.6.

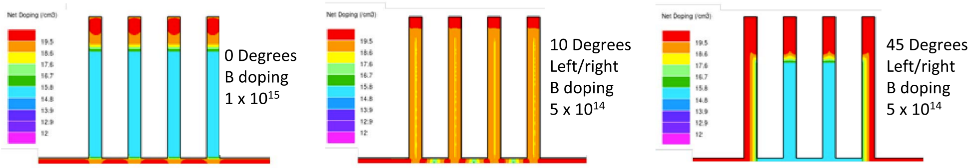

Figure 1.6: *Ion implantation simulation on densely packed nanowires at three different angles. (a) A 0 degree angle produces a heavy level of doping on the nanowires tip, leaving the rest undoped; (b) a double, half-dose doping with a 10 degrees angle on both sides results in a low sidewall doping and lacks uniformity with the nanowires tips; (c) a double, half-dose doping at 45 degrees from both sides suffers from shadowing effects between nanowires. Image taken from [21].*

In the figure, the researchers show how, in a close-packeted nanowire array, the achievement of conformal and uniform doping profiles is hindered by the geometry of the system itself. As a matter of fact, in figure 1.6a, the doping from 0 degree angle results in the enrichment of the nanowires tips and in the absence of impurity atoms on the sides; in figure 1.6b, with a left and right 10 degree angle doping, the nanowires are doped in a non-uniform fashion; finally, figure 1.6c shows the case of a left and right 45 degrees doping, in which central nanowires are shielded by the lateral ones, and the resulting doping profile is hampered by shadowing effects. Since the semiconductor industry approach, as mentioned before, is shifting towards the exploitation of nanoarchitecture-based devices, the adaptation of existing doping techniques to these systems may answer to the needs of current technology, but the introduction of new, more versatile and more suited doping strategies like MD will allow for a better exploitation of new nanostructures designs and their doping.

Chapter 2

Literature review on Molecular Doping

2.1 Introduction to Molecular Doping

Recently, the improvement of device performances had to be based on new, innovative strategies, involving the use of nanostructures with unique optical, physical and electrical properties. This can be seen in a plethora of attempts and successes on the fabrication of nanostructured devices like nanowire-based solar cells [22] and MOSFETS [23], carbon nanotubes sensing devices [24] and fin- structured FETs [10]. The greater the shift towards these technologies, the more important becomes the need for new doping methodologies with two fundamental characteristics: conformality of the doping profile and precise control of the dopant dose. A new doping method with these two characteristics has been presented by Javey and his group in 2008 [13] in the article "Controlled nanoscale doping of semiconductors via molecular monolayers", called MonoLayer Doping (MLD) or, more recently, Molecular Doping (MD). The method consists in the deposition of dopant-containing molecules from liquid phase. The substrates are immersed into a solution, kept at its boiling point, made of a molecular precursor and a solvent. During this step, usually of 150 minutes, precursor molecules form a self assembled layer on top of the sample surfaces. The samples are then subjected to an annealing process in which the deposited molecules decompose and release the dopant atoms to be diffused into the substrates lattice, with kinetics typical of the diffusion phenomenon, introduced in chapter 1.2.3. The whole process is summarized in figure 2.1.

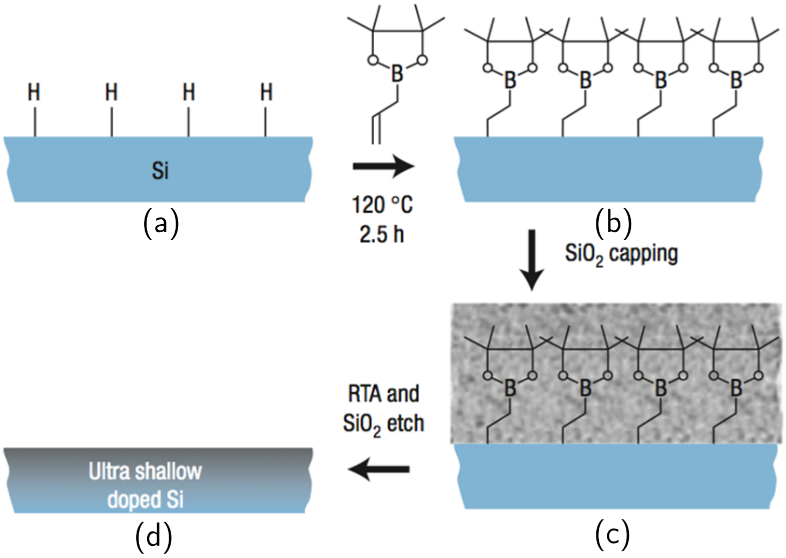

Figure 2.1: *Diagram of the doping process presented by Javey and his group [13]. The technique starts with the cleaning the sample surface (a), the molecular precursor is deposited on it and forms a self assembled layer (b), the sample can then be covered by an oxide layer cap (c). Afterwards, the thermal annealing allows the dopant to be released and diffused into the sample, and a doped substrate is obtained (d).*

In the same article, Ho et al. demonstrate how the final results of the process can be modeled by tuning the process parameters. Results are shown in figure 2.2. In particular, while figure 2.2a and 2.2b show the modification of electrical properties by the tuning of annealing temperature and time, figure 2.2c shows how the resulting sheet resistance can be controlled by mixing the molecular precursor, during the deposition step, with a "blank" molecule (i.e. a molecule without dopant atoms).

Since its first appearance in 2008, the technique has been applied to many materials such as indium arsenide, oxidized silicon, alumina and mica [25, 26, 27, 28]. Metallurgical, 5-to-10 nm deep junctions with a dop-

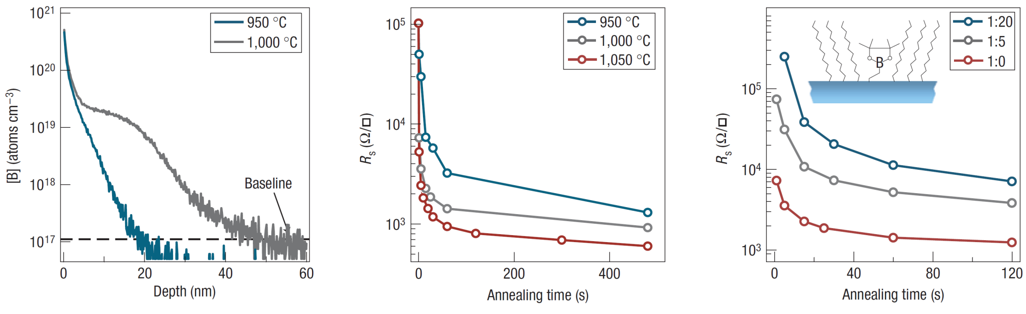

(a) (b) (c)

Figure 2.2: *[13] Secondary Ion Mass Spectrometry profiles (a) and sheet resistance vs annealing time (b) of MD-doped samples at different annealing temperatures. Figure (c) shows the possibility of modifying final sheet resistance of the samples by mixing the molecular precursor with "blank" molecules at different ratios during the deposition step.*

ing concentration of 10^{20} have been realized, both for the n and p-type doping [29, 30]. It has also been used for the doping of 4-inches silicon wafers [30], demonstrating its scaling capabilities for industry applications. These characteristics, along with the conformality of the doping profile and the control of the dopant dose will be discussed in the next sections, together with a few MD application examples.

2.2 Control of the doping properties

In silicon technology, doping concentrations range from 10^{15} to 10^{21} cm^{-3}, roughly corresponding to doses in the range between 10^{12} and 10^{18} cm^{-2}. The distribution of dopants is of fundamental importance for the functioning of the silicon-based devices. The wide range of applications of semiconductor doping requires a sharp control of the obtainable doping properties such as dopant diffusion depth, dopant concentration, dose and activation efficiency. In the MD process, the possibility of controlling such properties has been extensively explored. In particular, these characteristics can be tuned by modifying the MD process conditions: deposition time, temperature, solution parameters, choice of precursor molecule and annealing parameters. By its first introduction in 2008, the studies on the influence of annealing and solution characteristics had already been started, as shown in figure 2.2. Since then, other approaches have been explored which will be described in the following examples.

Mixed Self-Assembled monolayer strategy: Mixed Self-Assembled Monolayer (mSAM), which is obtained by the simultaneous adsorption from a mixed solution of two or more solutes and a solvent, a heterogeneous layer of two or more species of molecules can be obtained [31, 32, 33, 34]. Since the maximum avaiable dose in the molecular doping process is determined by the presence of the precursor molecule on the sample prior to the annealing step, the modification of its population leads to modified final electrical results of the doping itself. In the article in which MD has been introduced for the first time [13], the possibility of controlling the doping properties by a mSAM had been already explored. In this example, boron-doped Si substrates have been obtained by the use of Allyl Boronic Acid Pinacol Ester (ABAPE) as dopant source. To demonstrate the doping properties modulation by the use of mSAMs, Si substrates were put through MD deposition steps into solutions with a mixture of ABAPE (precursor molecule) and Dodecene ("blank" molecule) in different ratios: 1:0 (blank-free solution), 1:5 and 1:20 in volume. Electrical results, shown in figure 2.2c in section 2.1, confirm that resistivity is heavily dependent on the precursor/blank molecule concentration ratio and is further influenced by the annealing parameters, with the 1:0 case having the lowest sheet resistance and the 1:20 one having the highest of the three. This idea has been further explored in the work of Ye L. et al. [35]. In this work, the precursor molecules of choice (either ABAPE or Diethyl Vynil Phosphonate) were mixed with 1-undecene at various proportions, ranging from 100% (pure precursor molecule) to 0.1%. This mixture was then diluted in mesitylene at a volume ratio of 1:19 to be used as a MD deposition solution. In both cases, the surface presence of the precursor-molecule was investigated by XPS and Auger Electron Spectroscopy (AES), revealing that the ratio of precursor/blank molecules of the obtained monolayer depends on the initial mixing ratio. After the annealing process, dopant dose with a variation of 1 order of magnitude could be obtained, demonstrating how it can be controlled by the use of mSAMs.

Molecule chemistry and design choice: Precursor molecules occupy a region of space on a sample surface, corresponding to their steric footprint. The main consequence of this is that, since the samples represent a fixed surface area, a given amount of molecules can be packed together creating a SAM, dependent on their size. Since the introduction of MD, molecular footprint has been demonstrated to be a major factor in the determination of the final electrical properties of samples, with higher footprint resulting in lower dose [13]. The difference has been initially studied by the comparison of doped samples by using Diethyl-propyl-phosphonate (DPP) or Tri-Octyl-Phosphate (TOP). While DPP has a molecular footprint of 0.1 nm^2, TOP has 0.6 nm^2. The resulting dopant dose, estimated from the sheet resistance data were 7.9×10^{14} and 1.3×10^{14} respectively, demonstrating how the choice of the molecular footprint is a key aspect of the dopant dose control. Another molecular footprint comparison example can be found in the work of Caccamo S. and Puglisi R. A. [36], in which a Phosphoric Acid (PA), a carbon-free molecule, has been used in the process of MD for Si substrates. Results are shown in figure 2.3.

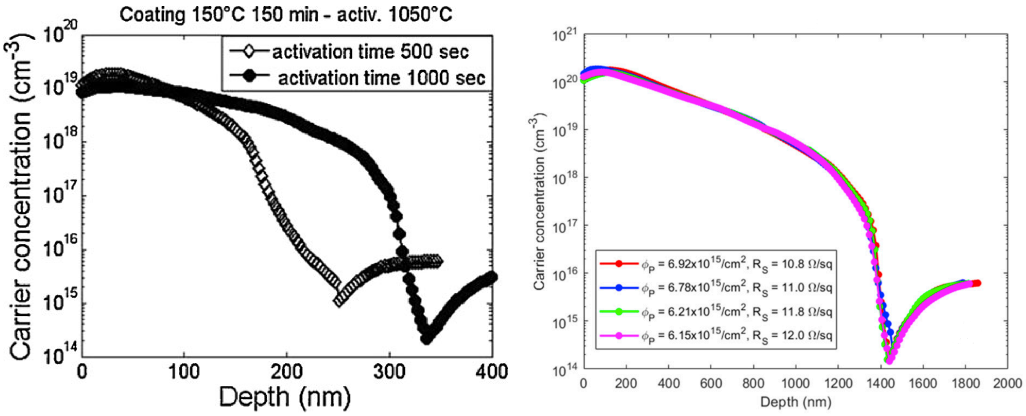

(a) (b)

Figure 2.3: *Spreading Resistance Profiling data of (a) DPP [37] and (b) PA [36] MD-doped samples. Even though samples have been similarly made, their carrier concentration reaches different peaks and junction depths:* 10^{19} *and* 10^{20}*, with a depth of around 300 and 1400 nm, respectively. This is due to the different molecular footprint of the deposited molecules.*

In both cases, the Si samples were kept inside a 20% concentrated solution of the precursor molecule in a solvent, and kept at the solution boiling point for 150 minutes. The annealing processes were then performed at 1050°C in N_2 environment for 500s and 1000s for the DPP case (figure 2.3a) and for 500s for the PA case (figure 2.3b). The maximum carrier concentration reached is of the order of 10^{19} with a junction depth of 300 nm by using DPP, while it reaches 10^{20} with a junction depth of 1400 nm by using PA as the precursor molecule. The simulated molecular structure of the PA molecule is shown in figure 2.4 (image taken from [36]). As it is shown, the PA molecule bond extensions are 0.25 nm for the single P-O bonds and 0.14 nm for the double P=O bond. In comparison, the DPP molecule exhibits a maximum lateral extension of 0.9 nm and a minimum lateral extension of 0.7 nm [38]. This is a paramount aspect of molecular design choice in MD, because it ensures a denser packing during the molecule self-assembling process of the PA molecule, thus leading to a higher molecular/dopant density on the Si surface prior to the annealing step, effectively raising the dopant atom dose at the start - and at the end - of the diffusion process.

It is important to notice that molecule design affects also other aspects of the process. Firstly, the molecule-substrate interaction depends entirely on the nature of both: different substrates can be doped by MD with the right choice of the precursor molecule. Moreover, in Si substrates, the presence of carbon atoms has been demonstrated to reduce the doping efficiency of phosphorus [39], which can be avoided with the use of carbon-free molecules.

2.3 Examples of applications

In chapter 1.4, some of the bottlenecks of current doping techniques have been presented. The main issues are related to the doping of small nanostructures in a conform and uniform fashion and keep their functional shape during the process. In literature, examples of similar systems being doped with the MD technique can be found [22, 13, 40, 41, 42]. In particular, in the work of J. Veerbeek et al. [40], three doping methods have been tested in order to achieve the doping of porous-nanowires ar-

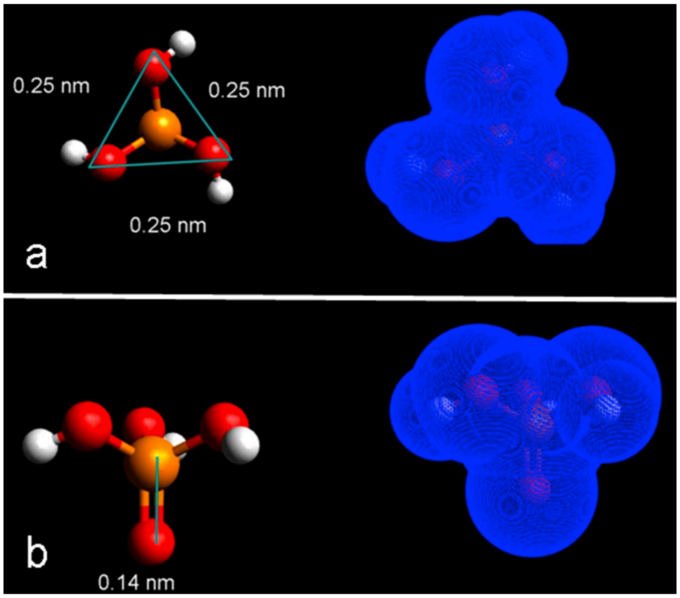

Figure 2.4: *Evaluation of molecular footprints of PA [36] showing profiles of the single bonds (a) and the double bond (b) between phosphorus and oxygen atoms. Simulation data indicates that the maximum extension of the PA molecule is 0.25 nm.*

rays: MD, contact MD and a combination of the two. The use of either MD or contact MD is succesful in providing a dose between 10^{14} and 10^{15} atoms/cm^2, while the combination of the two led to a doping dose of 10^{17} atoms/cm^2 in a highly porous nanowires system, while leaving the nanoarchitectures intact. Moreover, the precursor molecules have been observed while attached to the sidewalls of nanowires after treating them with the MD deposition process [38].

Hollow structures can also be doped by MD. R.A. Puglisi et al. report on microhole-patterned structured silicon being doped with boron atoms by AllylBoronic Acid Pinacol Ester (ABAPE) molecules through the MD process [37]. Afterwards, the samples have been subjected to a beveling process in order to be analyzed in cross section. Images are shown in figure 2.5.

The figure shows (a) the FIB section SEM images of the prepared samples and (b) the Scanning Capacitance Microscopy map of the cross sec-

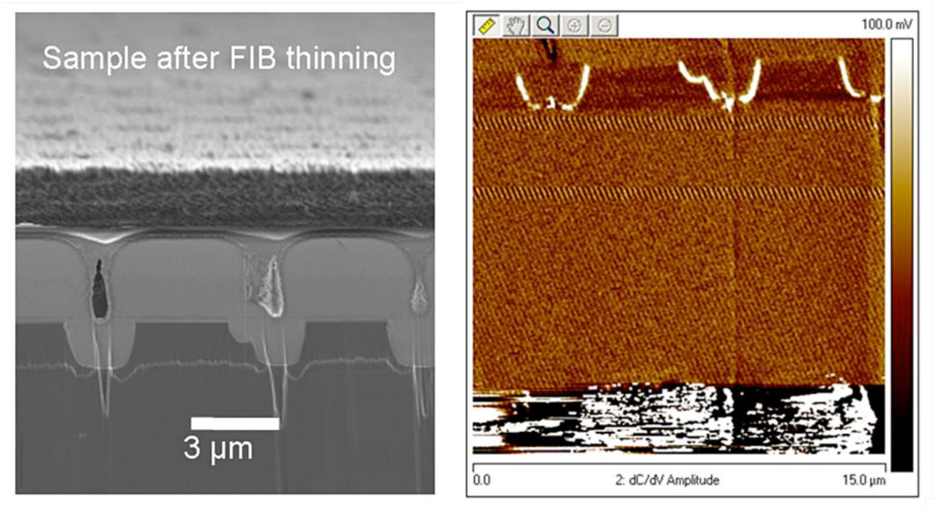

(a) (b)

Figure 2.5: *(a) Cross section SEM image of the microhole patterned sample. The image shows the hole Si structures after the MD doping process has been completed and the holes have been filled with a SiO_2 layer. (b) SCM map of the micro patterned sample. In this image, the bright lines correspond to the doped regions of the Si. The image demonstrates that the doping profile follows the shape of the micropattern [37]*

.

tion in which the conform doping of the hollow structures is demonstrated.

The capability of MD in the doping of nonplanar architectures can be exploited in device design and production. Shortly after its introduction to the scientific community, reports of ultra-shallow doping of substrates have been made, together with the demonstration of its scalability to industrial applications [30]. Subsequently MD has been recognized by the scientific community as a candidate doping method for the manufacture of modern FET and CMOS devices based on fins, nanowires and other nanoarchitectures [28, 43], even more so since the damage-free doping of a finFET structure was achieved [44], while similarly made structures were heavily damaged by an equivalent ion implantation process.

By combining its conformality with its ability to dope nanostructures, the conformal shell doping of nano-fin structures has been also achieved [45]. Solar cells have also been fabricated by MD. The use of micro- to nanometer-scale structures has been demonstrated as a way to achieve a higher harvesting efficiency of p-n junction solar cells, by dramatically increasing their surface-to-volume ratio and thus, as a consequence, their photon capture capability [41]. Examples of this can be found in the work of Garozzo et al. [46, 47], in which microhole-patterned solar cells were fabricated and subsequently doped with MD, and Puglisi et al. [22], in which Si-NWs have been produced on a p-doped substrate samples and a p-n radial junction has been fabricated with the use of a phosphorus-containing precursor molecule in the MD process.

Chapter 3

Literature on the molecular nucleation processes

The MD process is based on the properties of the interface between the molecules and the substrate, but also on the characteristics of the molecules arrangement and clustering on the target surface. In particular, the precursor molecule deposition step occurs via the nucleation and growth of the molecule clusters on the sample to be doped. The process of nucleation and the related phenomena are then an important aspect in the MD process. For this reason, in this chapter the nucleation free energy, the critical radius and the nucleus growth process will be explained through the classical nucleation theory.

3.1 General nucleation theory

3.1.1 Homo- and hetero-geneous processes

The process through which a new phase of a given monomer (atoms, molecules, molecular assemblies, ions, etc...) forms within an initial, different phase of the same monomer, called phase change, starts with the phenomenon of nucleation. This phenomenon begins when two or more monomers stick together in clusters of the new phase, called nuclei embryos. If the phase transition is thermodynamically favoured, the embryos will grow in size into the new phase, which will be represented by a configuration with lower free energy than they had before the phase change. Since the change into the new phase (from here on called phase β) happens within the initial phase of the monomer (from here on called phase α), the smallest possible cluster of phase β into phase α will necessarily be formed by monomers mostly at the interface between the two phases. These surface monomers are in a higher energy state then the others and thus, energy is *needed* to form a new phase β nucleus: it requires work (W). Bigger clusters with a higher number of monomers (which will be called n) have a smaller fraction of monomers at the interface, and require less work to be formed. The relation between work needed to form a nucleus, the surface energy of the nucleus and the number of monomers that constitutes it can be derived by thermodynamics fluctuations first described by Gibbs [48]. In this perspective, the probability of a *relevant fluctuation* (i.e. random deviations of a system from its state, that occur in a system at equilibrium) is proportional to the entropy associated with the change in available states for a small volume of monomer medium δS:

$$P = Cexp(\frac{\delta S}{k_b}) \tag{3.1}$$

$$\Delta S = k_b \ln \frac{w_\beta}{w_\alpha} \tag{3.2}$$

In which C is a constant, k_B is the Boltzmann constant, w_β and w_α are the number of available states in phase β and α respectively. If W_{min} represents the minimum work required for the formation of a nucleus, equation 3.1 can be rewritten as:

$$P = Cexp(\frac{W_{min}}{k_B T}) \tag{3.3}$$

With T temperature in absolute units. An expression of W_{min} can be derived by calculating the energy change ΔU between phase α and the formation of a cluster of phase β within phase α. Consider the formation of a droplet in a gaseous medium without external interactions, in an isothermic system. Let the gaseous medium be enclosed inside a frictionless adiabatic piston, shown in figure 3.1.

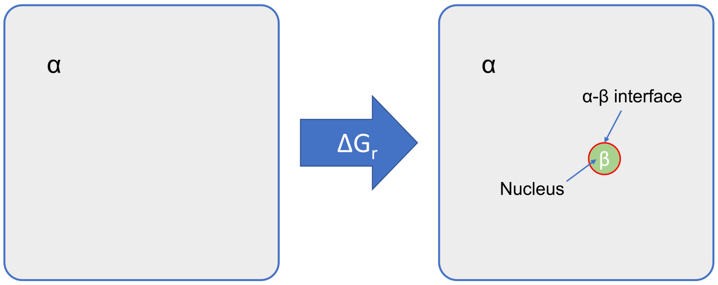

Figure 3.1: *Representation of the creation of a phase β nucleus within phase α. Energy (ΔG_r) is required in order to form the nucleus and its surface.*

With the subscript '0' describing the system in the initial state and the subscript '1' describing the system after the formation of the droplet. Let the pressure p_0 acting on the piston be constant. If N_{ij}, V_{ij} and p_{ij} are, respectively, the number of monomers, the volume and the pressure of the phase j in the system i, the energy difference of the system associated with the formation of the droplet can be written as:

$$\Delta U = U(S_1, V_1, N_1) - U(S_0, V_0, N_0) \tag{3.4}$$

Which, by expanding the internal energy into their single contributions becomes:

$$\begin{aligned}\Delta U = ((-p_0 V_{1\alpha} + TS_{1\alpha} + \mu_{1\alpha} N_{1\alpha}) + (-p_0 V_{1\beta} + TS_{1\beta} + \\ \mu_{1\beta} N_{1\beta} + \sigma A) - (-p_0 V_0 + TS_0 + \mu_0 N_0)\end{aligned} \tag{3.5}$$

Where μ_{ij} is the chemical potential, introduced because there's an exchange of monomers between phases, p_i, N_i, S_i, V_i and μ_i are the total parameters of the system i (constituted by the sum of their phases' parameters), A is the surface area of the interface between the phases. Note that μ_{ij} is a function of pressure and temperature of the phase j in system i and, for the sake of the ease of reading, it will not be specified unless necessary. Assuming the total number of atoms is conserved, ΔU can be rewritten as:

$$\begin{gathered}\Delta U = (-p_{1\beta} + p_0) V_{1\beta} - p_0 \Delta V + \\ T\Delta S + \sigma A + N_{1\beta}(\mu_{1\beta} - \mu_1)\end{gathered} \tag{3.6}$$

With $\Delta V = V_1 - V_0$. Given this, the change in Gibbs free energy between the systems can be described as:

$$\begin{gathered}\Delta G = \Delta U + p_0 \Delta V - T\Delta S = \\ (-p_{1\beta} + p_0)V_{1\beta} + N_{1\beta}(\mu_{1\beta} - \mu_{1\alpha}) + \sigma A\end{gathered} \tag{3.7}$$

Since it has been assumed that the formation of the cluster is a reversible transformation of the system, $S_0 = S_{1\alpha} + S_{1\beta}$. By introducing the two following equations:

$$\begin{gathered}Laplace\ equation : p_{1\beta} - p_0 = \frac{2\sigma}{r} \\ Gibbs - Duhem\ equation : SdT - Vdp + Nd\mu = 0\end{gathered} \tag{3.8}$$

And by noting that at a constant temperature $SdT = 0$, these results can be derived:

$$\begin{gathered}N_{1\beta}(\mu_{1\beta}(p_{1\beta}, T) - 1\beta(p_0, T) = \frac{2\sigma}{r} V_{1\beta} \\ \Delta G = N_{1\beta}(\mu_{1\beta}(p_0, T) - \mu_{1\alpha}(p_0, T)) + \sigma A = N_{1\beta}\Delta\mu + \sigma A\end{gathered} \tag{3.9}$$

In this equation, $\Delta\mu$ represents the change in chemical potential related to a single molecule changing phase from phase α to β. For this system we can then identify the minimum work needed for cluster of n monomers to be formed:

$$W(n) = n\Delta\mu + \sigma A \tag{3.10}$$

While the second term of this equation is always positive, since it's the energy needed for a surface between phases to form, the first one, which is a volume term, might not be. As a matter of fact, when $\Delta\mu$ is negative, the phase transition is favoured: the surface energy scales with $n^{\frac{2}{3}}$, while the volume of the cluster scales with n. For a sufficiently large cluster, the minimum work required for cluster formation becomes negative. The energy barrier for the formation of a cluster in shown in figure 3.2.

If we call $\Delta G_V = n\Delta\mu$, the energy required for the cluster's smallest volume change dV, and $\Delta G_S = \sigma A$, the energy required for the cluster's smallest surface change, both obtained by the addition or subtraction of a monomer, the equation 3.10 can be rewritten into:

$$W(n) = \Delta G_V + \Delta G_S = \Delta G \tag{3.11}$$

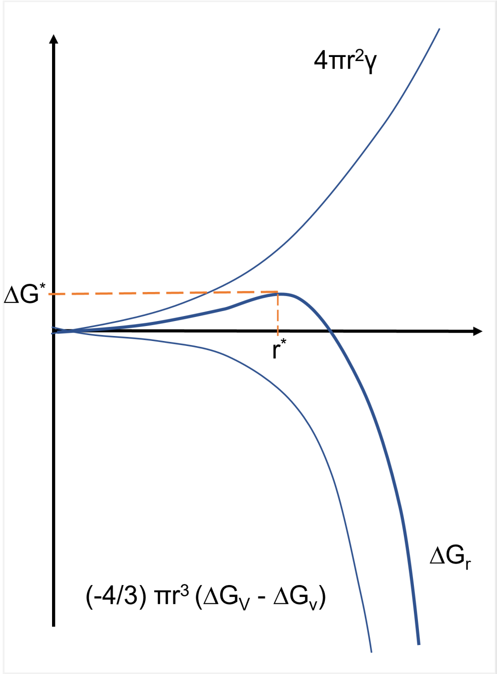

Figure 3.2: *Free energy of a nucleus during its formation. Critical free energy of nucleation* ΔG^* *and critical radius* r^* *are indicated.*

For a spherical cluster of radius r, the terms can be written as:

$$\Delta G = 4\pi r^2 \sigma + \frac{4\pi r^3}{3} \Delta G_v \tag{3.12}$$

Where ΔG_v is the free energy change per unit volume without the surface energy, the relationship between $W(n)$ and the radius of the cluster r can be expressed. With this notation, the value r^*, shown in figure 3.2 can be identified as the radius beyond which the magnitude of the two energy terms is exchanged, called the critical radius. By minimizing ΔG of the system with respect to the number of forming clusters, the equilibrium concentration of the clusters of size r (the number of clusters per unit volume that contain n molecules) can be written as:

$$\begin{aligned} N_r^{eq} &= N_0 exp(-\frac{\Delta G_r}{k_b T}) \\ N^* &= N_0 exp(-\frac{\Delta G^*}{k_b T}) \end{aligned} \tag{3.13}$$

With N_r^{eq}, N^*,ΔG_r and ΔG^* being, respectively, the number of clusters of size r and r^* and the free formation energy of a cluster of radius r and r^*, N_0 being the number of monomers per unit volume. Moreover, since r^* can be obtained by minimizing ΔG, these expressions can be obtained:

$$\frac{\delta(\Delta G)}{\delta r} = 0; \quad r^* = |\frac{2\sigma}{\Delta G_v}| \quad \Delta G^* = \frac{16\pi\sigma^3}{3(\Delta G_v)^2} \tag{3.14}$$

Nucleation rate, defined as the number of formed nuclei per unit volume and unit time can be written down as follows:

$$I = \nu N^* \tag{3.15}$$

Where ν is the frequency with which an additional adjacent monomer adds on to a critical nucleus by a diffusive jump at the $\alpha - \beta$ interface. By considering the system at a fixed temperature T, we can expand ν and thus, I as follows:

$$\begin{aligned} \nu &= \nu_0 exp(\frac{-Q}{k_b T}) \\ I &= N_0 exp(\frac{-\Delta G^*}{k_b T}) \nu_0 exp(\frac{-Q}{k_b T}) \end{aligned} \tag{3.16}$$

Where N^* is expressed as in eq 3.13, where Q is activation energy for diffusion.

Since the phase β is formed within the phase α, this process is called *homogeneous nucleation*. *Heterogeneous* nucleation refers instead to the phenomenon of nucleation in presence of a catalyzing element, an inhomogeneity, usually represented by a surface or an extraneous grain onto which monomers can form the new phase. The phase change energy barrier is usually easier to overcome than in the homogeneous case. From an experimental point of view, nucleation is almost always realized though inhomogeneities: free surfaces, container walls, sample surfaces and others which act as favorable sites of nucleation. The critical work for heterogeneous nucleation will be expressed as ΔG_h^*. The contribution of the interface onto which the nucleation occurs will be mostly seen into the energy required for the nucleus formation, since the interface will introduce a positive free energy. To demonstrate so, let us consider an inert

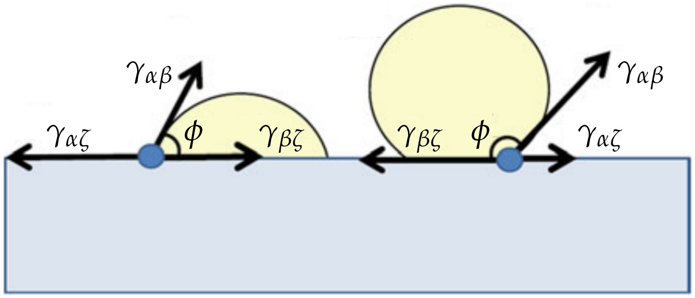

Figure 3.3: *Surface orientations* $\gamma_{\alpha\beta}$, $\gamma_{\alpha\zeta}$ *and* $\gamma_{\beta\zeta}$ *which define the contact angles between phase* α, β *and the substrate* ζ *in two different examples. Image adapted from [49].*

interface ζ that will act as the nucleant inhomogeneity, while the phases in contact with ζ will be phase α and β as mentioned in previous sections. Surface contact energies can be defined for each pair: $\sigma_{\alpha\beta}$, $\sigma_{\alpha\zeta}$ and $\sigma_{\beta\zeta}$. When $\sigma_{\alpha\beta}$ is greater or equal to the difference between the other two, both α and β phases can be simultaneously in contact with ζ, and the contact angle ϕ can be calculated:

$$\begin{aligned} \sigma_{\alpha\beta} &\geq |\sigma_{\alpha\zeta} - \sigma_{\beta\zeta}| \\ \sigma_{\alpha\beta}\cos\phi &= \sigma_{\alpha\zeta} - \sigma_{\beta\zeta} \end{aligned} \tag{3.17}$$

In general, at equilibrium, the more stable phase nucleates as a spherical cap, but it is not the only possible shape. Any anisotropy of interfacial energy can modify the ideal spherical cap shape producing, for example, lenticular shapes at the interface between two liquids [50]. If the contact angle is small, the spherical cap might not be the best description of the nuclei shape, while the "pill" shape is a much better approximation. Regardless of particular cases, let us consider spherical cap nuclei of the phase β growing on ζ from phase α. If the curvature radius of the spherical cap is r, its volume and its interface surface with phase α can be calculated as follows:

$$\begin{aligned} V_{sc} &= \pi(2 - 3\cos\phi + \cos\phi^3)\frac{r^3}{3} \\ A_{sc} &= 2\pi(1 - \cos\phi)r^2 \end{aligned} \tag{3.18}$$

Which can be written, respectively, as the volume of a sphere with radius r multiplied by a factor $f(\phi) = \frac{1}{4}(2 - 3\cos\phi + \cos\phi^3)$ and the surface of the same sphere multiplied by a factor $a(\phi) = \frac{1}{2}(1 - \cos\phi)$. The area between ζ and phase α is the area of the circle delimited by the spherical cap cluster. $\alpha - \beta$ and $\beta - \zeta$ interfaces are created at the cost of the $\alpha - \zeta$ interface. With the use of equation 3.17, we can write the energy required for this exchange:

$$\Delta G = (\frac{4\pi}{3}r^3\Delta g + 4\pi r^2\sigma_{\alpha\beta})f(\phi) \tag{3.19}$$

where Δg is the α-to-β Gibbs free energy change per unit volume of the nucleus. By minimizing ΔG, an expression for r^* similar to the homogeneous case can be derived which in turn lets us derive an expression for ΔG_h^*:

$$\begin{aligned} r^* &= -\frac{2\sigma_{\alpha\beta}}{\Delta g} \\ \Delta G_h^* &= \Delta G^* f(\phi) \end{aligned} \tag{3.20}$$

Since $0 < f(\phi) < 1$, the ΔG_h^* is reduced with respect to his homogeneous counterpart, which means that nucleation is favoured in the heterogeneous case with respect to the previous case. The contact angle is very influenced by phase β interaction with the surface. For example, $\phi = 0$ if the surface is made of the same phase as the nucleating monomer, and the nucleation barrier is reduced to a minimum.

If a solution is supersaturated, it eventually will nucleate regardless of the critical nucleus size or the presence of a surface. To understand how supersaturation influences the nucleation rate, the following relations must be taken into consideration:

$$\begin{aligned} \Delta\mu &= k_b T c \\ \Delta G_v &= \frac{\Delta\mu}{\Omega} = k_b T\frac{c}{\Omega} \end{aligned} \tag{3.21}$$

where c is the degree of supersaturation and Ω is the unit volume per molecule. As a consequence, we can express ΔG^* as follows:

$$\Delta G^* = \frac{16\pi\sigma^3}{3}(\frac{\Omega}{k_b Tc})^2 \tag{3.22}$$

which highlights the importance of the degree of supersaturation in the determination of the nucleation rate. In particular, the critical Gibbs free energy is proportional to c^{-2}.

3.1.2 Incubation time, growth and coalescence

In this section, two aspects pertaining to the phenomenon of nucleation will be introduced: the nuclei incubation time and the nuclei growth.

Nuclei incubation time: The time required to be able to experimentally observe the first nucleus, usually referred to as incubation time or lag-time, can be expressed as follows:

$$\tau_{inc} = \tau + \tau_g \tag{3.23}$$

where τ is the time required for the formation of a stable nucleus, while τ_g is the time required for a stable nucleus to be of detectable size. While only τ_g is influenced by the instrument used for the nucleus detection, both of the terms are influenced by the nucleation thermodynamic parameters like temperature, pressure, whether the nucleation is hetero- or homo-geneous, degree of supersaturation, etc. In the case of steady state nucleation (eq. 3.16), the dependency of τ from these parameters can be easily be expressed by the relation:

$$\tau \propto \frac{1}{I} \tag{3.24}$$

It is worth mentioning that in the case of time-dependent regimes, the nucleation rate must be expressed as $I(t, T)$, both a function of time and temperature. In this case, the induction period can be extracted by evaluating the integral of the nucleation rate over time to 1:

$$N(\tau) = \int_0^{\tau} I(t, T)dt = 1 \tag{3.25}$$

In-depth analyses with explicit time-dependent forms of $I(t, T)$ can be found in the works of F.C. Collins, D. Kashchiev, H. Wakeshima and J.W.P. Schmelzer [51, 52, 53, 54].
Nuclei growth: After the nucleus formation, the nucleus can grow in size. The growth rate of a nucleus depends on its dimensionality (2D or 3D), on the degree of supersaturation and other thermodynamic parameters. For a generic phase transformation α to β, two main regimes are recognized: the interface controlled growth and the diffusion controlled growth. In the first case, the growth is controlled by the rate at which the monomers can attach at its interface. Approximately, the growth rate g_r is proportional to the monomer interface diffusion coefficient as $g_r \propto D = D_0 exp(-\frac{Q}{k_b T})$, and the nucleus radius increases linearly with time. This is often the case of the same monomers arranging into different phases of the same material (example: $\alpha - \gamma$ phase changes in polymorphic iron). In the second case the transformation requires a change in monomer composition as well as an adaptation to the new phase's crystal structure. This regime is called diffusion controlled because the nucleus growth rate depends on the diffusion of the α phase monomers within itself in order to reach the interface. In this case, the nucleus radius increases parabolically with time. It is worth noting that if there is a difference in monomer orientation between phases, anisotropic growth can be observed, leading to the formation of one-, two- or three-dimensional structures. In the case of liquid droplets on a substrate, the growth behaviour is also affected by the wetting behaviour of the nucleating species on the surface which, in turn, is determined by the difference in liquid-liquid and liquid-solid chemical and physical interactions. If the cohesive forces between the nucleating monomers are stronger than the adhesive force with the surface the growth tends to develop in 3-D (island growth), while if the surface adhesive forces are stronger, the growth tends to develop in 2-D (layer by layer).

3.2 Molecule nucleation from liquid phase

3.2.1 Physisorption and chemisorption of species

In figure 3.4 the most elementary processes that happen during molecule deposition on a surface are represented, which can be summarized in: i) Adsorption; ii) Diffusion; iii) Desorption. In this paragraph, general notions on these processes are introduced.

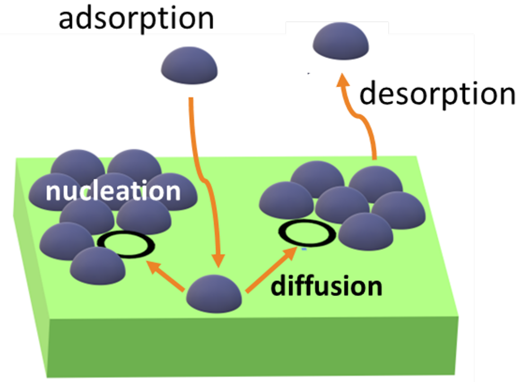

Figure 3.4: *Representation of the elementary processes involved in the deposition of monomers on a substrate.*

Adsorption: The adhesion of a monomer (atoms, ions or molecules) onto a surface from a gas or liquid phase is called adsorption. When the monomer approaches the substrate surface it is influenced by the mutual interaction, which depends on the specific nature of the adsorbate and the substrate. In the MD process, the adsorption of the precursor molecules on the surface sample results in the formation of the SAM, prior to the annealing step. If the molecules arrive to the surface with a rate R and χ represents the percentage of molecules from the impinging flux to be adsorbed, then the adsorption probability can be expressed as $p = R\chi$. While the adsorption of gases on a solid usually involves the interaction of one species with the substrate surface, the adsorption from solution always includes a competition between the solvent and the solute at the interface. Adsorption can result from physical interactions or chemical ones, and, as a consequence, is broadly classified into two categories -

physisorption and chemisorption. To summarize, the most distinguishing factors between physisorption and chemisorption are [55]:

- Physisorption is a general phenomenon with a relatively low degree of specificity.

- Chemisorbed molecules are linked to reactive parts of the surface and the adsorption is necessarily confined to a monolayer. At high relative pressures, physisorption generally occurs as a multilayer.

- A physisorbed molecule usually keeps its identity and, after desorption occurs, returns to the fluid phase in the same state as the initial one. Instead, the chemisorption must provoke a chemical reaction with the substrate and thus a chemisorbed molecule usually loses its identity and can hardly desorb from the surface.

- Chemisorption requires an activation energy: low temperature systems may not have enough thermal energy to stimulate the chemical reaction. Physisorption systems generally do not require energy to overcome a barrier.

In figure 3.5, the simplest case of potential energy of a adsorbed species in relation to its distance to the surface is presented. In the picture, the physisorbed state and the chemisorbed state are separated by a conversion energy barrier E_{conv}, and the adsorption states potential wells have depths E_p and E_c, respectively. Generally speaking, the molecule-substrate distance is typically around 1-3 Å in the chemisorbed case and 3-10 Å in the physisorbed one.

Diffusion and Desorption: Once on the substrate surface, the molecule can either move on it by jump to neighboring adsorption sites, if available (diffusion), or reach the free state again (desorption). Both of these processes have an activation energy, since the molecule has to overcome the potential wall of physi- or chemi-sorption. A simplified potential diagram is shown in figure 3.6.

The characteristic time of both processes can be described as follows:

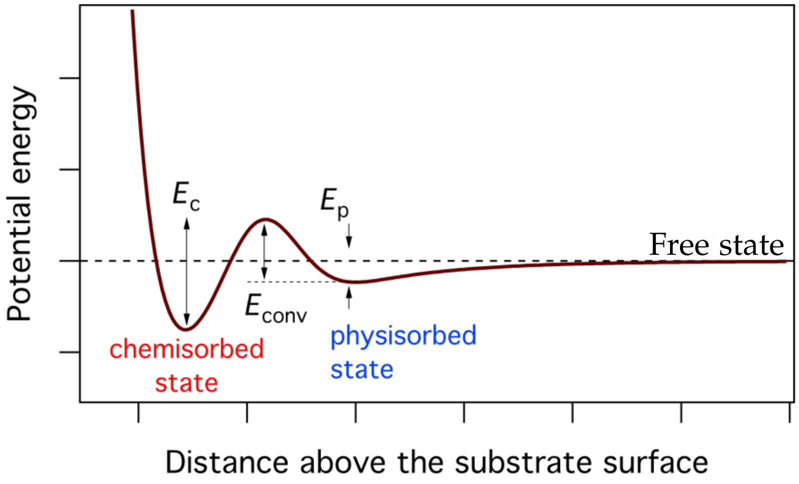

Figure 3.5: *Chemisorption and physisorption potential energy diagram. Potential wells have a depth of E_c and E_p, respectively, and are separated by an energy barrier of hight E_{conv}. Adapted from [56].*

$$\begin{aligned} \tau_{diff} &= \nu_{diff}^{-1} exp(\frac{E_{diff}}{k_b T}) \\ \tau_{des} &= \nu_{des}^{-1} exp(\frac{E_{des}}{k_b T}) \end{aligned} \tag{3.26}$$

Where E_i and ν_i are the activation energy and the pre-exponential factor of the respective processes. While τ_{diff} can be interpreted as the average time a molecule takes to hop from an adsorption site to another, τ_{des} can be interpreted as the average surface residence time of an adsorbed molecule, and the inverse of these quantities are the molecule diffusion and desorption frequencies per unit time. With these two quantities, the diffusion coefficient D and the average molecule walk distance λ can be evaluated:

$$\begin{aligned} D &\propto \frac{l_{diff}^2}{\tau_{diff}} \\ \lambda &= \sqrt{D\tau_{des}} \end{aligned} \tag{3.27}$$

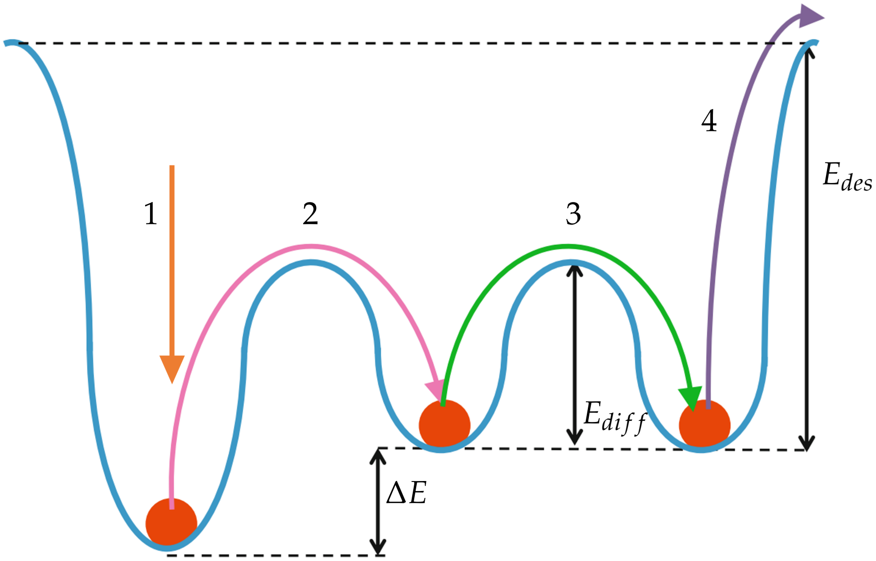

Figure 3.6: *Potential diagram of a molecule on a solid surface. Elementary processes and their activation energies are represented: 1) Adsorption; 2) Escape from an adsorption site; 3) Diffusion jump; 4) Desorption. Modified from [49].*

With l^2_{diff} being the length of the diffusion jump. The diffusion length λ represents the average distance passed by the molecule on the substrate before it desorbs. It is worth mentioning that the characteristics of the substrate are a fundamental aspect for the evaluation of the rates of adsorption: irregularities, kinks, steps or boundaries of growing islands represent preferred adsorption sites and reduce the values of τ_{diff} and λ.

3.2.2 Transient and direct molecular nucleation

In the previous section, the elementary phenomena occurring at the molecule-surface interface during nucleation have been presented. Each process (chemi- or physi-sorption, diffusion and desorption) can be described by characteristic quantities as time constants and activation energies. If n_0 is the total number of surface physisorption sites and n_p is the number of physisorbed precursors, then $\Theta = n_p/n_0$ can be defined as the coverage of available physisorption states. By taking into consideration the processes of physisorption and desorption, the surface density of physisorbed molecules n_p can be derived by the following [57, 58]:

$$\frac{dn_p}{dt} = R\chi n_0(1-\Theta) - \frac{n_0\Theta}{\tau_{des}} \tag{3.28}$$

Where $p = R\chi_p$ is the probability of physisorption and the term $\frac{n_0\Theta}{\tau_{des}}$ defines the desorption rate of physically-bound molecules. If we also take the possibility of chemisorption and its time constant τ_{chem} into consideration, the previous relation can be modified into:

$$\frac{dn_p}{dt} = R\chi n_0(1-\Theta) - \frac{n_0\Theta}{\tau_{des}} - \frac{n_0\Theta}{\tau_{chem}} \tag{3.29}$$

This simple model already highlights a feature of the adsorption process: the population of physisorbed molecules depends on the balance between the time constants τ_{des} and τ_{chem}. If τ_{chem} is very short, the population of physisorbed molecules decreases rapidly with time in favor of the chemisorbed state, and the molecule adsorption process can be considered as a direct chemisorption from the free state. If τ_{chem} is long, then the physisorbed molecule may not be able to thermalize to a bound state immediately, and can diffuse on the surface as a 'hot precursor' [57]. In this case, the total probability of chemisorption can be expressed as:

$$p(\Theta) = p_0(1 + \frac{\Theta}{1-\Theta}\kappa)^{-1} \tag{3.30}$$

in which κ^{-1} corresponds to the average number of surface sites jumps made by a molecule prior to its chemisorption. A thorough demonstration of the equation can be found in the work of A. von Keudell [58]. The hot precursor state can thus be described as a short lifetime species that resides on the substrate surface which can either change state into chemisorption or desorb, and is, as a consequence, a *transient* state.

Precursor states in the molecular adsorption have been studied extensively in literature, and the effects of their presence have been demonstrated in many system such as CO adsorption on transition metals [59, 60, 61], formic acid on Cu(110) [62, 63] and others [64, 65, 66, 67].

3.2.3 Avrami equation

The isothermal phase transformation, from phase α to phase β, can be described by the Avrami model, also called the Johnson-Mehl-Avrami-Kolmogorov equation. The derivation of this model starts with two assumptions: (1) nuclei form randomically throughout the phase-changing material, with a nucleation rate I and (2) nuclei grow isotropically, i.e. uniformally in all directions, with a constant growth rate g. It is necessary to mention that two important factors are being ignored at this stage of the derivation: (i) the nuclei cannot form where the phase change has already happened and (ii) that, after some time, nuclei will impinge with each other, preventing further growth. These two factors will be implemented later in the derivation of the model. Given the volume of the material V, by taking into account these assumptions, the number of *spherical* nuclei dN^* forming during an infinitesimal time dt^* can be expressed as:

$$dN^* = IVdt^* \tag{3.31}$$

After a period of time t, the formed nuclei will have a radius r and a volume v as follows, which can be used for the evaluation of the total transformed volume of phase α into phase β during the infinitesimal time dt^* as follows:

$$\begin{aligned} v &= \frac{4}{3}\pi r^3 = \frac{4}{3}\pi g^3 (t-t^*)^3 \\ dV^* &= vdN^* = \frac{4}{3}\pi g^3 (t-t^*)^3 IVdt^* \end{aligned} \tag{3.32}$$

By integrating dV^* over the time variable, the total transformed volume over time can be obtained:

$$V^* = \int_0^t dV^* = \frac{1}{3}\pi g^3 iVt^4 \tag{3.33}$$

The quantity V^* is called 'extended volume', i.e. the total transformed volume over time ignoring conditions (i) and (ii). The 'extended fraction' of transformed volume can then be written as:

$$f^* = \frac{V^*}{V} = \frac{1}{3}\pi g^3 it^4 \tag{3.34}$$

It must be noted that this quantity is an overestimation of the transformed fraction, since conditions (i) and (ii) are not yet included in the calculations. At this stage, the overestimation can be corrected simply by noting that the fraction of volume in phase α, i.e. available for the phase transformation, can be expressed as $(1-f)$. As a consequence, the 'real' infinitesimal transformed fraction df can be calculated as follows:

$$\begin{aligned} df^* &= \frac{df}{(1-f)} \\ f^* &= \int_0^t \frac{df}{(1-f)} = -\ln(1-f) \\ f &= 1-\exp(-f^*) = 1-\exp(-\frac{1}{3}\pi g^3 i t^4) \\ \Rightarrow f &= 1-\exp(-kt^4) \end{aligned} \tag{3.35}$$

Which is the Avrami equation with a rate constant k and exponent 4. Note that this exponent actually derives from the assumption of spherical nuclei, which defines their volume as proportional to r^3 and, thus, t^3. Moreover, the growth rate of the nuclei is considered constant, which is a verified condition in most interface-controlled phase changes. Since the nuclei shape of a given phase β depend on the characteristics of the phase itself, the Avrami equation can be adapted to these cases by changing the initial expression of their volume in eq. 3.32. Simple examples include the 2 dimensional disc-shaped nuclei case and the 1-D nuclei growth for which the time exponents are 3 and 2, respectively. In the diffusion controlled growth regime, the Avrami exponent takes the values of 2.5, 2 and 1.5 for spherical, plate-like and needle-like nuclei formation and growth [68]. In general, this exponent is a pure number, independent of temperature, that describes the overall dimensionality of the phase change process. By generalizing eq. 3.35, the following can be written:

$$f = 1-\exp(-kt^n) = 1-\exp(-(\frac{t}{\tau})^n) \tag{3.36}$$

With n called the Avrami exponent, k called the rate constant, and $\tau = k^{-\frac{1}{n}}$ is called the time constant which is the time corresponding to a transformed fraction $f = 1-\exp(-(1^n)) = 0.37$. Since it first was demonstrated and presented to the scientific community, the Avrami equation has been used extensively for the deduction of phase transformations mechanisms that occur via nucleation and growth. However, the assumed conditions at the base of the theory are rarely fulfilled experimentally [69]. As a matter of fact, unusual values of n can be found widely in scientific literature [70, 71, 72, 73]. For example, transient nucleation and heterogeneous nucleation conditions give rise to modifications of the classical Avrami exponent values, with $n > 4$ associated to transient behaviours and $3 < n < 4$ owing to heterogeneous nucleation. An in depth study of the relation between the non-classical values of n and the underlying nucleation mechanisms can be found in the work of I. Sinha and R. K. Mandal [73]. Moreover, the incubation time τ_{inc}, introduced in section 3.1.2, can be implemented in the Avrami equation as follows:

$$f = 1 - \exp\left(-k(t - \tau_{inc})^n\right) \tag{3.37}$$

in which the time origin is shifted by an amount proportional to the incubation time [74].

Chapter 4

Experimental studies on the molecule adsorption

In chapter 2, MD has been described as a doping technique involving roughly three steps: (i) the sample surface cleaning, (ii) the precursor molecule SAM formation and (iii) the thermal treatment to stimulate the dopant diffusion. These three steps are performed in sequence but separately from each other. This gives the possibility to investigate, understand and improve each the MD steps, taken singularly. Since the MD deposition step defines the dopant reservoir from which the dopant impurities can diffuse in the semiconductor, its mechanisms are an important aspect to be addressed, especially if in relation to the obtained semiconductor electrical properties. In this work the molecule deposition step is evaluated through morphological, computational and electrical considerations. The recognition and study of the first and second layer of molecules is performed. Although the investigation of molecular multilayer formation during the deposition has been performed in the past [75, 76], however, a systematic study on their formation has not been presented so far. Direct observation at high-resolution of the deposited molecular layers has not been done. This work shows the direct observation of the molecules morphology over time, the multilayer formation, and the effects of post-deposition treatments on them. We study the surface coverage of Diethyl-Propyl Phosphonate (DPP) at 10 % dilution and the morphology of the aggregates over the Si substrate by Scanning Electron Microscopy (SEM). We corroborate these results with Density Functional Theory (DFT) simulations of the grafted molecule over Si, which has been observed in a previous work [38]. We present these data together with electrical measurements of carrier concentration depth profiles produced with the MD process at different synthesis conditions by Spreading Resistance Profiling (SRP).

4.1 Experimental methods

Si samples, 1×1 cm^2 1-10 ohm/sq <111> p-type, have been employed for this study. Prior to the molecule deposition, the samples have been cleaned in HF. The molecule deposition step has been carried out in a 10 % concentrated (v/v) DPP (Abcr, 95 %) and Mesitylene (Abcr, 98+%), kept at the solution boiling temperature for the desired time, ranging from 7 to 150 minutes. The samples have been divided into two groups, one to be analyzed right after the deposition (*as-deposited* samples), the other to be cleaned with a surface treatment consisting in rinsing in acetone, ethanol, water, and stirring in acetone with a magnetic stirrer for 15 minutes (*cleaned* samples).

Scanning Electron Microscope (SEM) analysis was performed by a Zeiss Supra 35 FE-SEM (Oberkochen, Germany), with a primary energy beam of 3keV. The SEM images extracted the surface coverage data by calculating fast fourier transforms (FFT) of the images, applying a proper bandpass filter mask on it, and calculating the inverse FFT of the filtered transforms obtained [77]. This method ensures a noise reduction of the images and allows for the recognition of the areas to be measured by determining a threshold in the electron intensity spectrum distribution over which the areas are recognized and measured. All measurements and calculations have been done with Digital Micrograph 3. The images resolution allowed for the recognition of clusters down to 32 nm^2 (6.4 nm diameter, assuming clusters as circular).

Spreading Resistance Profile (SRP) data were collected to calculate the carrier dose of a few samples after a rapid annealing process at 1050°C for 500 s in N_2 environment. The technique consists in using two metallic probes to measure a resistance profile of a beveled sample with an electric potential of 5 mV. Resistance is converted into resistivity and, with the use of calibration curves, carrier concentration and carrier dose can be calculated. SRP measurements have been carried out by a SSM150 tool.

4.2 Computational Methods

The simulations have been performed using density functional theory (DFT) implemented in the SIESTA code [78]. We employed the generalized gradient approximation (GGA) as formulated by Perdew-Burke-Ernzerhof (PBE) to approximate the exchange-correlation functional [79]. We applied the Monkhorst-Pack scheme [80] with $7 \times 7 \times 1$ k-points for sampling the Brillouin zone and a mech cut-off 300 Ry for the calculations. The atomic positions were optimized until the Hellmann-Feynman forces on the atoms were less than 0.05 eV/Å and the energy convergence threshold was 1×10^{-4} eV. We have modeled a silicon (111) surface with a 2×1 reconstruction using a slab of 24 atoms with 6.60 Å and 7.70 Å lattice parameters and 18.06 Å of the vacuum region to avoid interlayer interaction. The dangling bonds on the bottom surface have been passivated with hydrogen to prevent charge migration.

4.3 Results and Discussion

The investigation of the deposition step has been conducted in a 10 % concentrated (v/v) solution of DPP and Mesitylene, kept at its boiling point. The samples were immersed inside the solution and taken out after 7, 15, 25, 45, 60, 75, 120 and 150 minutes. After the deposition step, some of the samples did not undergo any other treatment («as-deposited» samples), while the others went through a surface cleaning process («cleaned» samples) consisting in rinsing with acetone, alcohol, and water, and 15 minutes magnetic stirring in acetone. SEM has analyzed both sample groups. Figure 4.1 shows the SEM plan images of the as-deposited samples with a deposition time of 7 (**a**), 15 (**b**), 25 (**c**), 45 (**d**), 75 (**e**), 150 (**f**) minutes. The surface coverage of each of these samples was measured over several images,and a mean value was calculated.

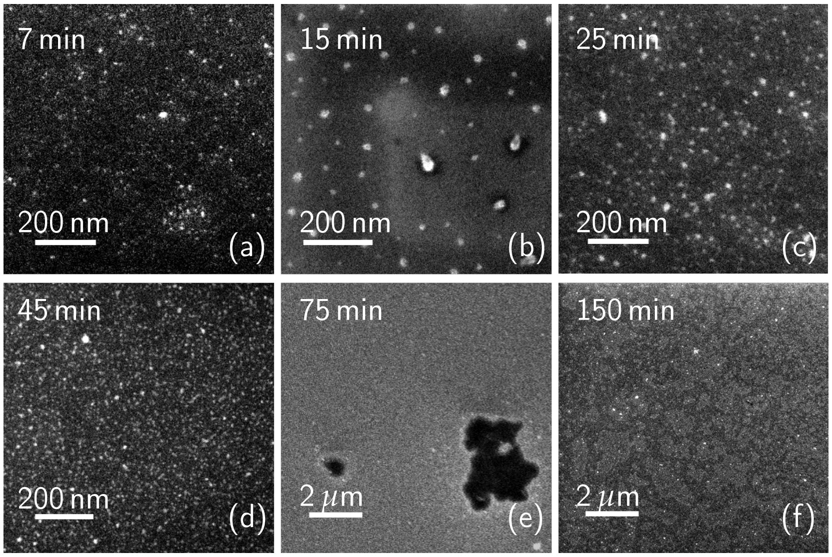

Figure 4.1: *SEM plan images of the as-deposited samples with a deposition time of 7 (**a**), 15 (**b**), 25 (**c**), 45 (**d**), 75 (**e**), 150 (**f**) minutes. Image (**e**) shows the molecular layer next to completion, while image (**f**) exhibits the presence of molecular terraces*

As it can be seen in Figures 1a, 1b, 1c, and 1d, the molecule cluster surface density grows as deposition time increases. The calculated surface coverage is 2.2 % (7 minutes sample), 5 % (15 min), 4.9 % (25 min), and 15.4 % (45 min), showing a significant increase between 25 and 45 minutes. At the 75 minutes mark (figure 4.1e), only a few dark areas can be seen. The measured surface coverage is 88.3 %. From this data, we can estimate a 100 % coverage value at about 100-120 minutes. The surface of the sample dip-coated for 150 minutes can be seen in figure 4.1f. The sample presents bright terraces, which could be seen as the first layer of DPP molecules, and the second layer of molecule terraces on top of the first. The surface coverage of this sample is then 149 %, indicating that there is a full, 100 % coverage first layer of molecules directly over the Si surface and the second layer of molecules covering 49 % of the first layer surface area. This data will be discussed later, together with the carrier concentration profile measurements. While the presence of multilayers and their removal from the top of the sample has been mentioned in many previous works [13, 81, 82], a deep investigation of the cleaning process effects on the molecule layers has not been done yet. In this work, the effects of surface cleaning on the molecule surface coverage have been investigated by cleaning a group of the produced samples right after the deposition step. Figure 4.2 shows the SEM plan images of the cleaned samples with a deposition time of (**a**), 15 (**b**), 25 (**c**), 45 (**d**), 75 (**e**), 150 (**f**) minutes. Again, the molecule surface coverage has been evaluated.

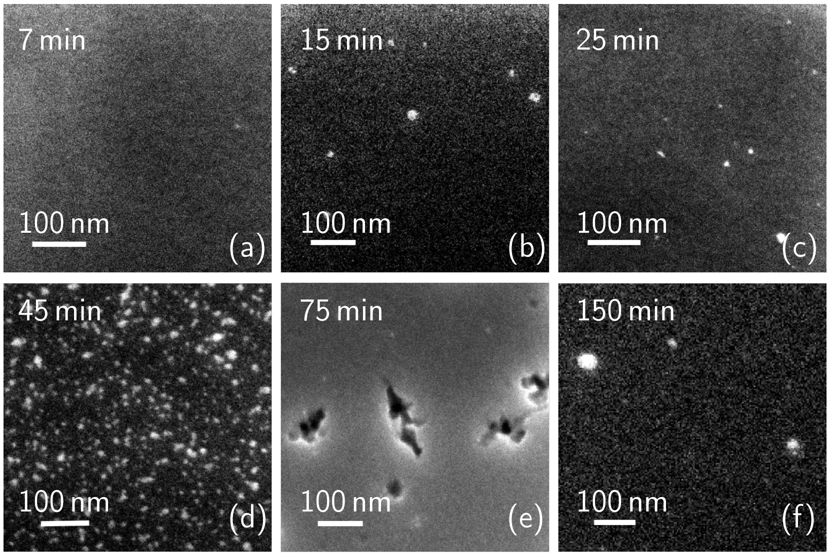

Figure 4.2: *SEM plan images of the cleaned samples at (**a**), 15 (**b**), 25 (**c**), 45 (**d**), 75 (**e**), 150 (**f**) minutes. The image contrast has been optimized to increase the signal-to-noise ratio.*

Despite the cleaning process, from the analysis, we observe that all the samples present the molecules on their surface, even though the surface density is lower with respect to the as-deposited samples, especially for the lower deposition times. Evidently, these molecules have not been removed by the surface cleaning process, which can probably be attributed to the chemical nature of their bonds with the Si surface. The sample dip-coated for 7 minutes (figure 4.2a) presents a surface coverage of 0.3 %. Figures 4.2b (15 min) and 4.2c (25 min) have a very similar morphology: both of these samples present sparse molecule nucleation spots, covering 3 % and 2 %, respectively. Figures 2d and 2e show a SEM plan image of a dip-coated sample for 45 and 75 minutes, respectively. The calculated surface coverage is 15 % (45 min) and 86.2 % (75 min), values in accordance with the same timestamp as-deposited samples (figure 4.1d and 4.1e) within experimental errors. This, together with the surface coverage data of other samples, will be discussed later on. Figure 4.2f shows the surface morphology of a 150 minutes dip-coated and cleaned sample. In this image, we can see that the surface appears mostly flat, with some molecule clusters with a bright appearance. The surface coverage of this sample is 103 %, accounting for a 100 % coverage molecule layer, plus a 3 % coverage of the molecule clusters over the first layer. This data will be discussed and confirmed later by discussing the carrier concentration profile data in figure 4.6. Surface coverage data from both sets of samples are represented in the graph of figure 4.3. In this image, blue dots represent data from the as-deposited samples, while orange squares represent coverage of the cleaned samples. Coverage over 100 % indicates the completion of the first layer and the deposition of a second layer on top of the first.

From the data in figure 4.3, it can be deduced that at the beginning of the deposition process, in particular up to the 25th minute, the deposition develops slowly. During these early stages, the surface coverage barely changes and, within experimental errors, tends to slightly increase, between 7 and 25 minutes. At 45 minutes, we can see that the curve starts to rise. The growth rate dramatically escalates between 45 and 75 minutes. From the comparison between the as-deposited and the cleaned samples, blue and orange data, we can deduce information on the bond type between the aggregates and the substrate. As it is evident, after the surface cleaning, the coverage dramatically drops, which could be representative of these bond types: chemical (thus strong) bonds and Van der Waals (thus weak) forces. Aggregates can be observed in both as-deposited and cleaned samples, even for low deposition times. Since simple cleaning processes hardly remove chemically bonded molecules, we can take these surface coverage measurements as an indirect quantitative evaluation of existing chemical bonds at the investigated deposition times. The data at 45 minutes shows that both the as-deposited and the cleaned samples present similar surface coverage within experimental errors. This could be an indicator of the fact that most of the present molecules in the as-

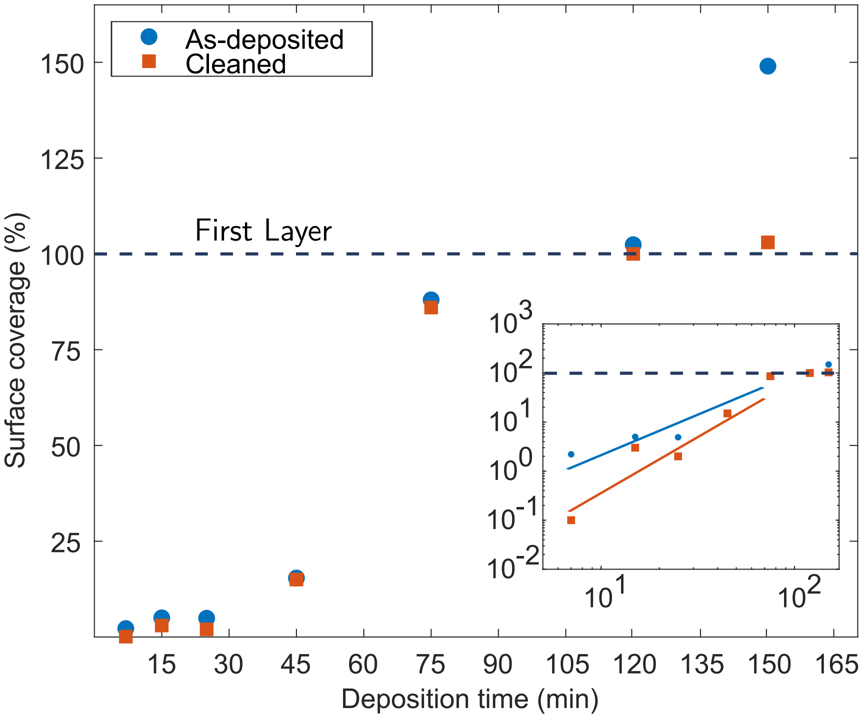

Figure 4.3: *Molecule surface coverage vs deposition time. Coverage values over* 100 % *indicate the completion of the first molecular layer and the growth of a second layer on top of the first one. Inset: log-log chart of the same data. Blue and orange lines are a guide to the eye. Coverage higher than* 100 % *indicates that a second molecular layer has been deposited on top of the first, which covers* 100 % *of the observed areas.*

deposited sample are chemically bonded. Regarding the bond formation mechanism, since the diffusion coefficient of a molecule depends on its mass [83] we start with the assumption that an aggregate of two or more molecules, independently on the forces keeping them together, could diffuse along the surface and that its diffusion coefficient diminishes as size increases, which has been thoroughly demonstrated for atomic clusters [84]. When this aggregate grows, its diffusion coefficient drops until the probability of a molecule group hopping from a bonding site to another reaches a minimum, and the chemical bond can be formed. A similar phenomenon involving the trapping of molecules into potential wells of temporary and long-lasting bonding sites is proposed in the work of R. Moiraghi et al. and its citations [85]. This explains the early stage of the deposition, in both cleaned and as-deposited conditions. The rapid increase in coverage, from the 45th minute on, is probably due to a switch in growth regime: in the first phases of the deposition, the creation of new molecular clusters occurs (nucleation phase), and the coverage increases slowly, while in the second part the created clusters tend to grow (growth phase) as described by the Avrami model [86]. When the second growth regime starts, molecules will have a significant chance to merge into an already existing cluster, come to a stop and form chemical bonds with the substrate since they are not diffusing anymore. The ratio between chemically bonded and physically bonded molecules becomes larger, hence the shrinkage of the difference in surface coverage between as-deposited and cleaned samples. As the first layer becomes complete, a second molecule layer starts to form on top of it. These newly deposited molecules will not be able to bond with the Si surface and will be physisorbed instead. The subsequent surface treatment removes the new layers: this explains the difference between cleaned and as-deposited samples in the latter parts of the investigated growth time. Nevertheless, further data and investigation are needed to understand more about the second layer formation. The inset in figure 4.3 shows the log-log chart of surface coverage data, with the lines drawn as a guide to the eye. The data of the as-deposited and cleaned data are systematically slightly different, with the cleaned ones lower than the as-deposited cases.

Figure 4.4 reports an example of the molecular complexes formed on the samples obtained after 15 minutes deposition and cleaning treatment. These structures are observable as well in the 45 min samples, after cleaning. The surface cleaning has probably uncovered the shape of these structures since physisorbed material could have deposited on top of them in an unshapely fashion, making it very difficult for the instruments to catch the detailed morphology underneath. We then speculate that, as described before, these structures are chemically bonded to the substrate. In figure 4.4a, two types of structure can be distinguished: terraces and linear branches. The minimum measured thickness of the linear branches is 8 nm, as indicated in figure 4.4b.

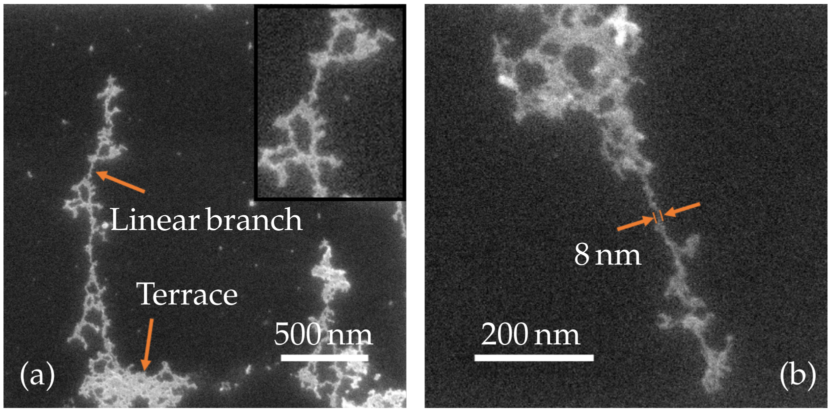

Figure 4.4: *SEM plan images of the samples dip-coated in a* 10 % *concentrated DPP solution for 15 minutes and cleaned after the deposition step. (**a**) Molecular branch and terrace, the inset shows a detail of the linear branch. (**b**) A thin, developed branch.*

To better understand these features and how the molecules are arranged inside them, we performed DFT calculations (see Methods section for technical details), providing information on the possible bond configurations. We covered the Si (111) 2×1 reconstructed surface by four broken DPP molecules in a way that three oxygens of the molecules initially bond with silicon atoms. The DPP molecule has been modeled without the aliphatic chains (-CH_2-CH_3) because we expect such a decomposition from previous Raman measurements performed on the samples after the molecule deposition [37]. It is not clear when the molecule loses these chains: it could happen either inside the solution or due to the interaction between the molecule and the substrate.

Figure 4.5 shows the optimized geometry of the molecules grafted on a Si (111) surface. As shown in the figure, the molecule assembles itself in packeted groups, which are chemically bonded with each other through P-O-P bonds and with the Si substrate through P-O-Si bonds, with an oxygen atom embedded into the Si surface. In principle, after the optimization process, the molecules located at the valley of the silicon surface were lifted to bond to the next molecules through oxygen. Our calculations reveal that the Si (111) surface structure was deformed due to the strain induced by the significant difference in atomic radius between em-

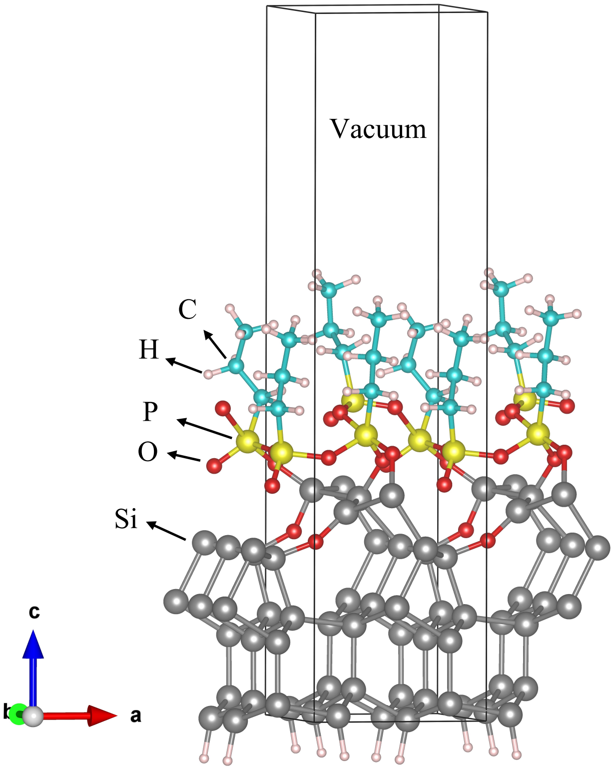

Figure 4.5: *Adsorption model of the grafted DPP molecules (without the aliphatic chains) on a Si (111) 2 × 1 reconstructed surface after DFT geometry optimization.*

bedded O (48 pm) and Si (111 pm) atoms. The longest Si-O bond forms with a length of only 1.78 Å, suggesting strong chemical bonds forming. Because of the strong adsorption between broken DPPs and Si atoms, the Si atoms were forced to move away from their initial positions. By comparing the DFT simulation results with the thinnest part of the branches in figure 4.4, we can estimate the number of molecules arranged in the thickness of the branch: since the simulated Si cell is 6.60 Å wide and there are two molecules per Si cell side, the thinnest part of the branch (8 nm thick) is made of about 24 molecules in a row. To evaluate the formation of the second molecule layer, we put the entire DPP molecule (28 atoms) on top of the first layer. The optimization process was carried out for positions with different vertical distances between DPP and the first layer (Figure 4.6). As shown in figure 4.6, the shortest distance between the second layer and first layer is 2.26 Å which is a relatively large distance indicating a weak interaction between DPP and the first layer. All the bond lengths of the DPP molecule show negligible changes before and after adsorption, revealing that a small charge transfer occurs between DPP and the first layer. These results demonstrate the weak physical adsorption of the DPP molecule as the second layer.

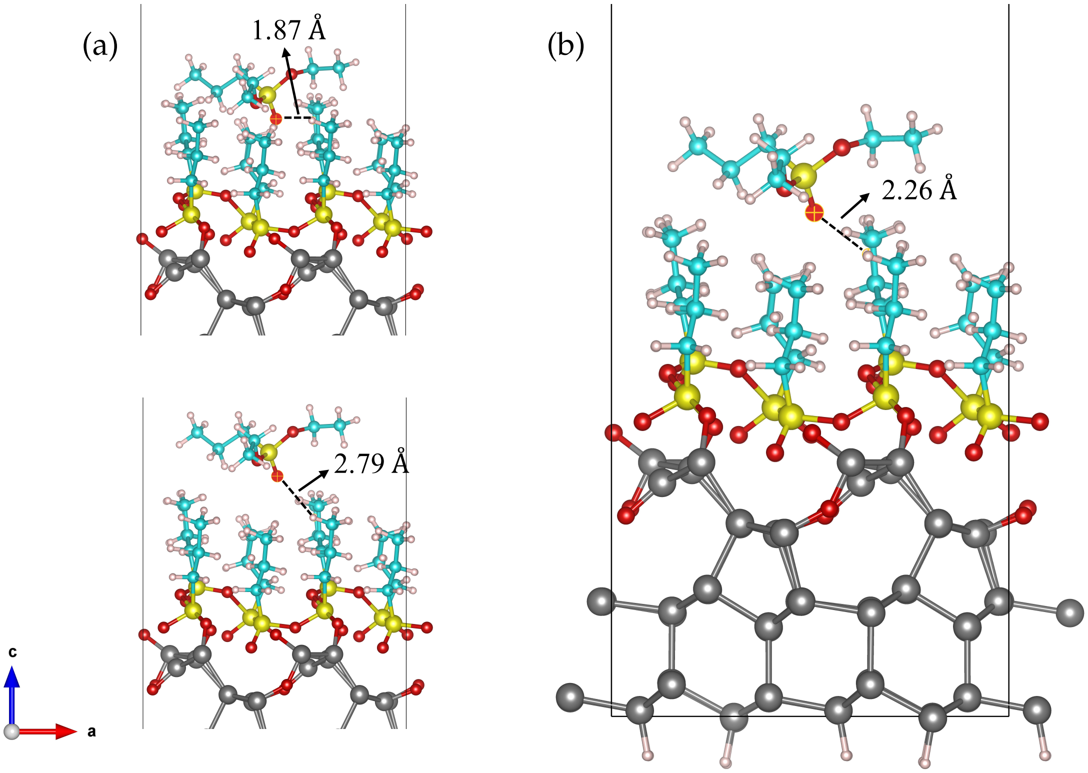

Figure 4.6: *(a) The initial DPP positions including shorter (top panel) and longer (bottom panel) vertical distances from the first layer and (b) the most stable structure of physisorbed DPP on a Si (111) 2 × 1 reconstructed surface covered by a broken DPP layer.*

After studying the molecules deposition process, we wanted to investigate the electrical properties of the samples. It is already known that by increasing the deposition time, in the 20 % as-deposited samples, i.e. without cleaning, the carrier dose and the junction depth increase monotonically, until a saturation condition is reached (at 100-150 min) [37]. In this paper, we present the electrical measurements of carrier concentration profiles at 150 min, i.e. in the saturation conditions where the full layer is deposited and the complete coverage is obtained, both for the as-deposited and cleaned conditions and compare the two cases.

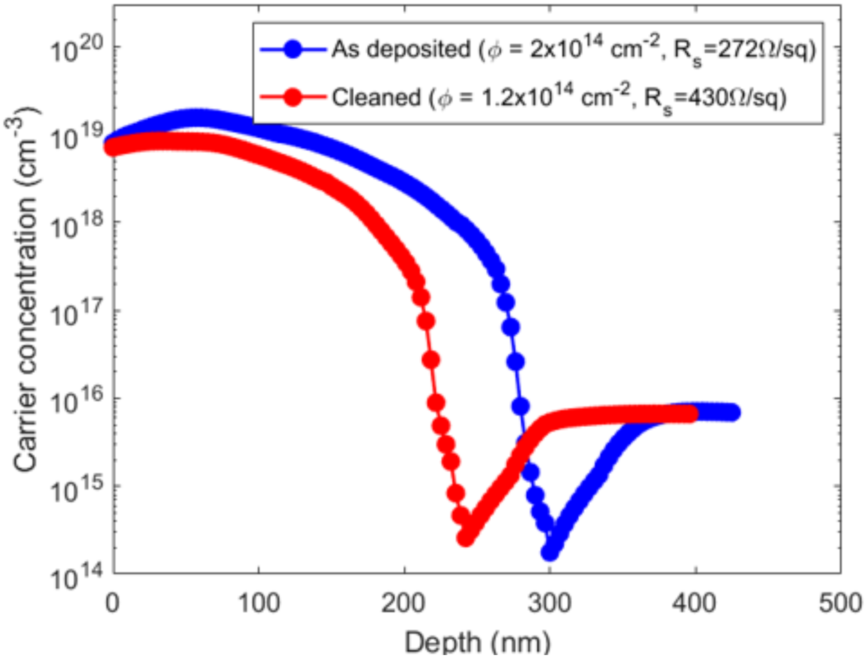

Figure 4.7: *Carrier concentration profile of the as-deposited (blue line) and cleaned (red line) samples with 150 minutes deposition in a* 10 % *concentrated solution.*

After the molecules deposition, we treated the samples with a thermal annealing at 1050°C for 500 seconds to diffuse the dopant inside the Si substrate. Figure 4.7 shows the electrically active carrier concentration profiles, obtained by SRP, of <111> Si substrates dip-coated into a 10 % concentrated solution for 150 minutes, i.e. in the saturation conditions, where the full layer is deposited, and the complete coverage is obtained, in two cases: as-deposited (blue line) and cleaned (red line). The graph shows that both the peak carrier concentration values reach 10^{19} cm^{-3}

with a junction depth of about 300 nm for the as-deposited case and of about 230 nm for the cleaned one. The carrier dose is $2 \times 10^{14}\#/cm^2$ (with a sheet resistance of 272 Ω/sq) for the former, and $1.2 \times 10^{14}\#/cm^2$ (with a sheet resistance of 430 Ω/sq) for the latter. The reason behind these results could reside in the role of physisorbed molecules in the diffusion process. Since the only difference between the preparation of the two samples is whether or not the samples surfaces have been cleaned, it can be deduced that not only the chemisorbed layer participates in the diffusion phenomenon, but also the physisorbed material. Since a richer dopant source is present on the surface of the as-deposited sample, the dopant dose is higher, and the resulting doping profile is deeper, as per the finite-source impurity diffusion behaviour [86]. By observing the electrical properties of these samples, we can confirm the presence of the molecular over-layers on the sample shown in figure 4.1f and of a single layer of chemisorbed molecules on the sample shown in figure 4.2f.

4.4 Conclusions

We investigated the behaviour of the DPP molecule at several stages of the deposition time during the MD process. The high resolution morphological data on the DPP surface coverage show that: i) the molecules form a full layer on top of the Si substrate after about 100-120 minutes of deposition; ii) a further layer of molecules starts to form over the first one. After cleaning the samples, the coverage decreases and this becomes more evident at long deposition times. By comparing the two sets of coverage data, the cleaned and the treated ones, we understand that there are chemical, thus strong, bonds between the first layer of molecules and the substrate, while the second layer is attached by weak bonds. To support these understandings, DFT calculations of the first layer of molecules on Si, and of the second layer over the first one have been performed. The simulations show that the DPP molecules of the first layer bond with the substrate through P-O-Si bonds, and with each other through P-O-P bonds. The simulations also indicate the weak nature of the forces between the second and first molecular layer. Electrical measurements performed on the cleaned sample with a full monolayer of molecules on top, demonstrate the efficiency of the doping method, even after cleaning. The comparison between as-deposited and cleaned samples electrical characteristics demonstrate how physisorbed molecules participate in the doping process, and how, with the use of a surface cleaning step, the dopant dose and doping profile can be further controlled, allowing for a finer tuning of the electrical properties of MD-based devices.

Chapter 5

Experimental study of the transient/direct molecular nucleation

As it has already been mentioned, MD involves the precursor molecule Swlf Assembled Monolayer (SAM) formation on the sample surface and the thermal treatment to stimulate the dopant diffusion. The literature on SAMs is very vast, and the applications, at the laboratory level, have been demonstrated in many cases, such as Li-batteries [87], transparent conductive oxides [88], for non-linear optics [89] and more extensively in biofunctionalized systems [90]. SAMs have also been applied to modify surfaces' electronic properties, where the SAM element represents the active dopant component [91, 92, 93]. In contrast to the last case, in the MD process the molecules represent the carrier for the dopant atom, not the active dopant element itself. For this reason, many of the technical requirements to give MD an industrial potentiality are relaxed with respect to the previously cited approach. Since the deposition step is made in liquid solutions, the resulting doping profile is conformal, i.e., it follows the shape of the sample surfaces from micro-sized systems, [94] to nano-sized ones [95, 96], with respective curvature radii of roughly 1.75 µm, 50 nm, and 5nm. Moreover, the possibility to produce highly doped (10^{20} cm^{-3}) metallurgical junctions with a thickness of 5-to-10 nm has been demonstrated, which makes the technique versatile and applicable to many geometries [97, 98, 44, 99]. Depending on the application, the desired doping dose in the Si industry spans within the wide range of 10^{12} - 10^{18} cm^{-2}. For this reason, the control on the MD efficiency has been explored thoroughly in the literature. Several studies have then been conducted on the dopant dose control, through the coating time [13, 37], the molecules footprint [13, 100, 101], the post-deposition surface cleaning process [102] or by diluting the deposition solution with a neutral molecule [103], i.e. not participating in the doping process. Studies of self-assembled molecular layer nucleation have observed how molecules can diffuse on the surface and tend to form ordered structures [104, 105, 106]. And this is further supported by the study on how the molecule sticks to the substrate, through which bonds and which orientation have the bonded molecules [96, 102].

Although the kinetics of molecule deposition and its relation to the deposition solution parameters have been studied in the past [40, 107, 108, 109, 110, 111, 100, 37], an in-depth study of the effects of the solution concentration on the final electrical properties of samples has not been done yet. The present work shows the morphological evolution of the diethyl-propyl-phosphonate (DPP) deposition on Si over time at several solution concentrations, the monolayer formation, and their comparison with the electrical performance of doped samples. We present these data together with a study of the monolayer formation evolution by analyzing surface coverage data with the Avrami function, which describes the temporal behavior of phase changes, and providing curve fitting on collected data, which will give insight into the behavior of the DPP-Si system at a molecular level [112, 113, 114].

5.1 Experimental methods

The employed substrates are 1x1 cm^2 1-10 ohm/sq p-type <111> Si samples. The molecule deposition was performed right after the substrates were sonicated in acetone, alcohol, and milli-Q water for 5 minutes each, then cleaned in HF for 1 minute. The deposition step has been carried out in 5%, 10%, and 15% concentrated (v/v) solutions of DPP (Abcr, 95%) and mesitylene (Abcr, 98%+). Samples and solution have been kept at the solution's boiling point temperature for the desired time. Samples were divided into two groups: one was treated with a surface cleaning process consisting in rinsing in acetone, ethanol, and water and stirring in acetone with a magnetic stirrer for 15 min ("cleaned" samples), while the other group ("as-deposited" samples) has been analyzed right after the deposition.

SEM images were taken with a Zeiss Supra 35 FE-SEM (Oberkochen, Germany) with a primary energy beam of 3 keV. The surface coverage has been extracted from these images using a noise reduction strategy based on the fast Fourier transform (FFT) filtering through an applied bandpass mask [77]. The inverses of the filtered FFTs were then transformed back by an inverse FFT. The application of a brightness threshold resulted in the identification of the interesting areas and the measure of surface coverage. Measurements and calculations were done with the Digital Micrograph 3 software. The contrast has been optimized to increase the signal-to-noise ratio. The image resolution allowed the evaluation of objects down to 32 nm^2 (or 6.4 nm in diameter if we assume circular cluster images). The developed image recognition process described above allows for noise identification and treatment, the proper choice of the object-identification threshold, and the image transformation from grayscale to black-and-white.

Thermal diffusion processes were performed in N_2 environment brought to 1050 °C for 500 s, with an initial ramp of 10 °C per minute, starting from 600°C. No oxide layer has been deposited on the sample surfaces before the annealing process.

Four-point probe sheet resistance measurements were performed using a Keithley 237 source-measure unit. Measurements were done in a dark environment to eliminate light-induced conductivity modifications on the samples. No metallic contacts have been deposited on the specimens to improve the electrical Ohmic contact between the probe and the semiconductor, so despite the measurements being consistent among the samples, they might present a systematic difference with respect to the results obtained with other electrical testing methods.

The Avrami function fits were performed by minimizing the least-squares errors between the Avrami equation (5.1) and the experimentally obtained surface coverage data, that is, we minimized the least squares error:

$$(t_{0,\text{opt}}, k_{\text{opt}}, n_{\text{opt}}) = \underset{(t_0,k,n)}{\text{argmin}} \sum_{k=1}^{K} \left[\frac{y(t_k) - F(t_k; t_0, k, n)}{\sigma(t_k)} \right]^2 ,$$

where $y(t_k)$ denote the experimental values at measurement times t_k, K is the number of temporal snapshots, $\sigma(t_k)$ are the corresponding measurement uncertainties (depicted as error bars in Fig. 5.4), and $F(t_k; t_0, k, n)$ denote the Avrami function values at times t_k, with respect to the parameters (t_0, k, n), as defined in (5.1). The overall fitness is represented by the (minimized) least-squares error, as stated in the last column of Tab. 5.1.

5.2 Results

We carried out the deposition step in a solution of DPP and mesitylene at different concentrations: 5%, 10%, and 15% (v/v). We kept the samples inside the solution at a constant temperature for times between 7 and 120 minutes. The samples were then divided into two groups: one group was subjected to a surface cleaning process consisting of a rinse in acetone, alcohol, and water, and 15 minutes of stirring in acetone (the "cleaned" samples), while the other group was not (the "as-deposited" samples). We analyzed the last ones by Scanning electron microscope (SEM) imaging. We selected SEM microscopy, which, in our case, exploited a field emission gun-based instrument providing high-resolution images because other techniques were not able to provide high-resolution morphological information on how the molecules are arranged and clustered. Figure 1 shows several SEM micrographs of the as-deposited samples for each series at different deposition times: figures (a) - (e) refer to samples produced in a 5% concentrated solution (5% samples), figures (f) - (j) are of samples obtained with a 10% concentrated solution (10% samples), figures (k) - (o) show samples dip-coated in a 15% concentrated solution (15% samples).

As can be seen from the images in figure 5.1, the molecular surface coverage of the three series of samples increases over time for all three solution concentrations explored. A nucleation phenomenon can be observed in figures 5.1a to 5.1d, 5.1f to 5.1h, and 5.1k to 5.1l, before the

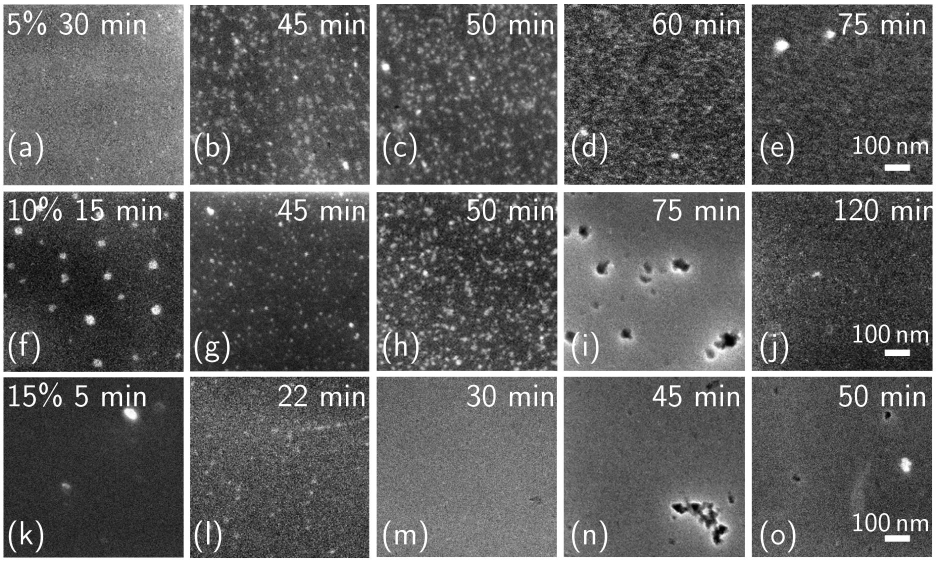

Figure 5.1: *SEM images of the samples at different deposition times. Each row of images refers to samples dip-coated in solutions of different concentrations: figures (a) - (e), 5%; figures (f) - (j), 10%; figures (k) - (o), 15%.*

impingement between the clusters and full coverage occurs. From a preliminary observation of the images, it is clear that the nucleation and the impingement appear to be heavily influenced by the concentration of the solution in which the deposition happens.

To be quantitative, we measured the surface coverage using the image analysis method described in the Materials and Methods section. We report the results in figure 5.2a), as a function of the deposition time. For the 5% samples, green symbols, the surface coverage goes from 0.9% after a 30-minute deposition to 63.8% after a deposition of 75 minutes; for the 10% samples, blue symbols, the measured surface coverage is between 2.2% at 7 minutes to a complete monolayer for deposition of 120 minutes; while for the 15% samples, red data, the surface coverage is 0.4% at 5 minutes and rises to an almost complete layer at 50 minutes. The dashed line indicates the 100% coverage. Coverage higher than 100% refers to a full monolayer coverage plus an additional coverage deriving from forming a second layer on top of the first. From the same image analysis, we also measured the nuclei surface density. We collected the results in the graph of figure 5.2b, where the molecular nuclei areal density vs. deposition time is represented for the 5% (green), 10% (blue), and 15% (red data) concentration. The arrows indicate the apparent decrease in nuclei density due to the impingement effect.

For the successive part of the discussion, it is essential to note that: i) the surface coverage increases more rapidly when the concentration increases; ii) for the high concentrations, the rate decreases at long deposition time, i.e., when the surface coverage reaches values larger than 80%; iii) the nucleation density and rate strongly depend on the solution concentration and iv) they increase with this parameter. Once the nuclei density behavior for several solution conditions was investigated, we intended to study the electrical properties of the final doped samples. For a deep comparison between the morphological characteristics and the sheet resistance results, however, it is essential to recall the previous knowledge on the interface between the molecules and the substrate. In previous work, we demonstrated how the molecular layers are constituted by molecules chemically and physically bonded to the substrate through, respectively, covalent and Van der Waals bonds [102]. In particular, at the end of the process, molecules of the first assembled layer are mostly chemically bonded to the Si surface. In contrast, molecules of the second layer are physically bonded to the first. Both molecules' layers contribute to the samples' electrical properties, but the last ones are easily removed from the surface after chemical treatment. It is then essential to evaluate how the changes in chemically and physically bonded molecules population reflect in the electrical properties of the samples. Consequently, it is necessary to study the samples' properties by removing the physisorbed molecules and compare the results with the physi- and chemisorbed cases. For this reason, we investigated the samples after the chemical treatment to remove the physisorbed component.

The data on the treated samples are reported in figure 3, showing the sheet resistance for the 15% (red), 10% (blue), and 5% (green) cases. The data evidence that the sheet resistance (Rs) systematically decreases with the deposition time, as expected, but also when the concentration decreases, i.e., the samples grown with diluted solutions exhibit better electrical conductivity. This contrasts the morphological data, showing a faster molecule coverage growth for the high solution concentrations.

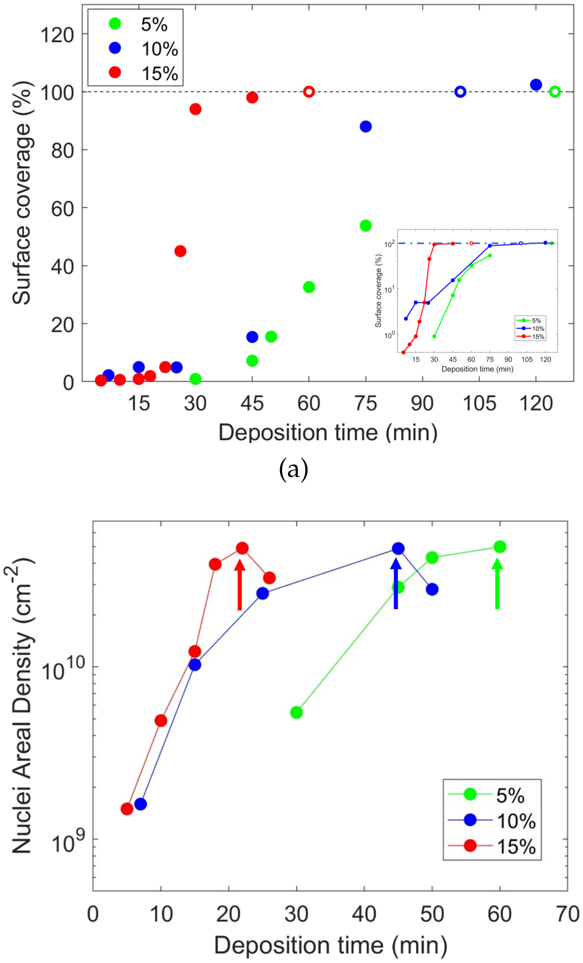

(a)

(b)

Figure 5.2: *(a) Surface coverage as a function of the deposition time. The dashed line indicates the 100% coverage. Coverage higher than 100% refers to a full monolayer coverage plus an additional coverage deriving from forming a second layer on top of the first. (b) Nuclei areal density of the samples vs. deposition time. The arrows indicate the nuclei density maximum value, after which there is a decrease due to the coalescence effect.*

Always in apparent contrast with the morphological data is the fact that at deposition times corresponding to the full or almost full coverage of the surface with the molecules (120min for the 5%, 80min for the 10%,

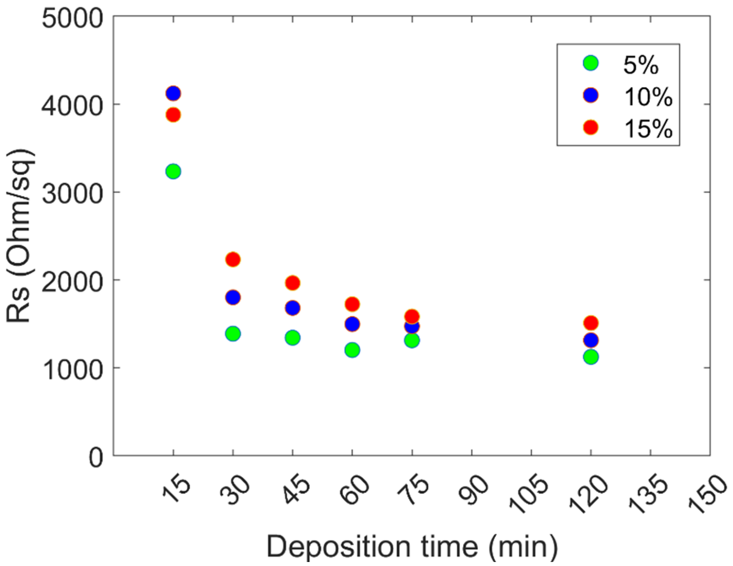

Figure 5.3: *Sheet resistance data of the samples of the 15% (red), 10% (blue) and 5% (green) sample series.*

and 30 min for the 15%), the Rs is still in the decreasing trend. Another aspect is that the sheet resistance difference among the three curves decreases as the deposition time increases, tending roughly to a common saturation value for the three solutions. Nevertheless, it should be noted that, at prolonged deposition times, there are still measurable differences between Rs values, with the diluted solution still showing the lowest resistance among the three. These results show that the solution concentration affects the electrical properties counter-intuitively, and the way the molecules interact with the sample surface must be deeply understood.

5.3 Fit to the data through the Avrami theory

To shed further light on the deposition process in the three cases, we use the Avrami function because it provides information on the dimensionality of the nucleation process of the molecule clusters.

We fit the surface coverage data to the Avrami function [112, 113, 114], defined by

$$F(t; t_0, k, n) = 1 - \exp\left(-\left(\frac{t - t_0}{k}\right)^n\right), \tag{5.1}$$

where $t > 0$ is the incubation time, k is related to the activation energy, and n is the Avrami exponent, associated with the dimensionality of the nucleation process [112, 113, 114]. The n exponent in the classical Avrami theory is an important parameter and represents the reason why we chose to use this theory to fit our data: n is equal to d+1, where d is the dimensionality of the phenomenon, so the 2Dimensional phase changes have an exponent of 3, and 3D ones have n = 4 [115]. When n is larger than 4, the literature refers to transient and nonlinear behaviors [70, 71, 72, 73], which represent the key element to understand the data and that will be discussed below. We used the weighted least-squares fitting for this task. We summarize the resulting parameters in Table 5.1 and showcase the functional fits in Figure 5.4. The very low value of t_0 in the 10% case could result from the process fluctuations at the early deposition stages. Moreover, despite the use of a high-resolution field emission gun - SEM microscope to acquire the images, the data collected through microscopy could not be accurate at the initial deposition stages for the following reasons: i) image resolution; (ii) in-homogeneity of the sample surface; (iii) Noise in the imaging process.

Table 5.1: Weighted least-squares fitting parameters.

Percentage [%]	t_0 [min]	k **[1]**	n **[1]**	**LS Error [1]**
5	6.53	68.18	3.86	9.70e-05
10	0.00	64.45	4.94	8.59e-04
15	11.50	15.73	6.66	5.99e-04

5.4 Discussion

The n's trend for the three series suggests a modification in the MD deposition nature. As said, the n exponent predicts the phenomenon di-

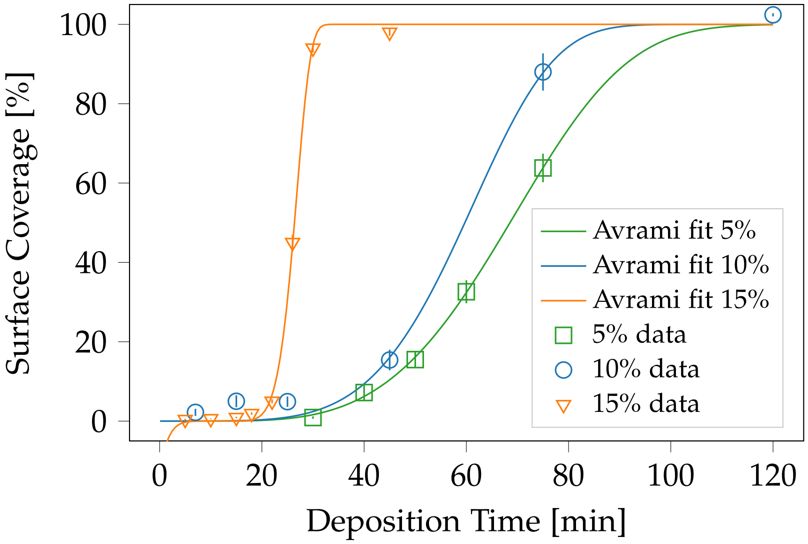

Figure 5.4: *Graph of the Avrami fits for the three sets of data: 5% in green, 10% in blue, and 15% in orange.*

mensionality. For n larger than 4, we know that we are in the case of transient nonlinear processes. In our case, n ranges between 3.86 and 6.66, increasing with the concentration, suggesting that these transient behaviors are more prevalent at high solution concentrations. In the case of nonlinear behaviors, two main types of deposition mechanisms have been evidenced in literature [57, 58]: the growth by direct adsorption, in which the deposited species directly develop a strong chemical bond with the deposited surface upon impinging on it, and growth via an adsorbed layer, in which an intermediate state of physisorption is involved between the desorbed and chemisorbed state. Our previous study shows that both sticking mechanisms are possible at the surface. But this study was experimentally performed at a specific solution concentration, and the simulations were performed on a small number of molecules [96, 102]. Nothing is known so far when the concentration varies and how large numbers of molecules aggregate. By considering these possible deposition and bonding mechanisms, an interpretation of the morphological data of figure 2 and their relation to the sheet resistance of figure 3 can be given. With a 5% solution concentration, the resulting Avrami exponent roughly matches the classical prediction of $n = 3$ for a 2-dimensional growth: even though the surface coverage is relatively low compared to the other cases at the same deposition time, the molecules develop chemical bonds upon impingement. They are not rinsed away by the surface treatment. In the 10 and 15% cases, the surface coverage follows a much steeper curve, with $n = 4.94$ and 6.66, respectively, indicating a change in how the molecules are deposited. The sheet resistance data for the 15% cleaned sample series, higher than the other cases, suggests that the physisorption is the bonding mechanism prevailing in this case. This is attributed to the high nucleation rate, which allows the physisorbed molecules to cover the surface with faster dynamics compared to those needed for the chemisorption. So at high concentrations, physisorption is the dominant mechanism in the physi-/chemi-sorption competition.

To understand why, with high molecular coverage, the 80% and above cases in Fig.s 1) and 2a), the sheet resistance at the corresponding deposition times is still decreasing, we have to take into account the spatial distribution of the molecule clusters and how the new molecules adhere to the substrate in the vicinity of a grown cluster. At high deposition times, when the coverage is large, another mechanism takes place, which can be explained by introducing the concept of the nucleus capture zone [77, 116, 117, 118, 119, 120, 121, 122]: molecules impinging on the surface around one nucleus are most likely to be captured by that nucleus and, thus, contribute to its growth. Each capture zone is approximated by the surface points closer to the nucleus center of mass than to other nuclei. Each nucleus capture zone depends as a consequence on the nuclei population around it [123]. This means that the faster the nucleation rate (high concentrations), the larger the total perimeter of the clusters formed on the substrate.

By nucleation and successive growth, molecular clusters keep forming on the sample surface. During the growth, the areas enclosed between the edges of these molecular clusters can present bonding sites in which the following deposited DPP molecule will not be chemisorbed but physisorbed. Figure 5.5 shows a process schematic. In the figure, a chemisorbed molecule is represented by a full-colored polygon. In contrast, the empty structures represent the surface areas where the depositing molecules can potentially be captured by a nucleus, identified by the

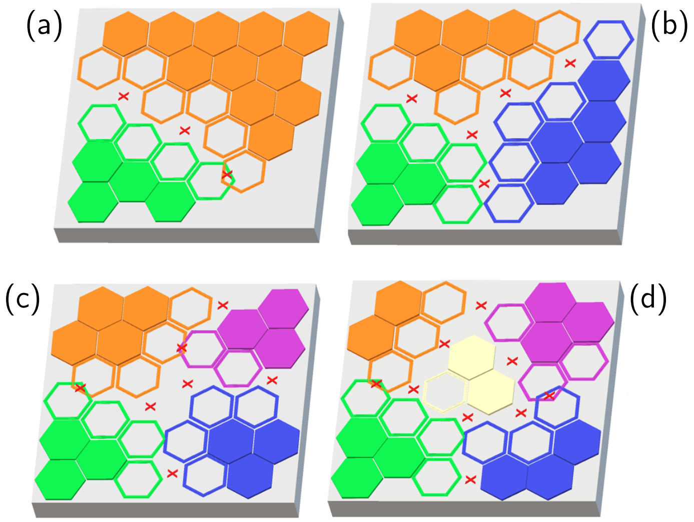

Figure 5.5: *A schematic of the relation between nuclei surface density and the surface zones available for chemisorption. In the picture, a chemisorbed molecule is represented by a fully colored shape. In contrast, an empty structure represents the surface spots where the depositing molecules could chemisorb when captured by a nucleus, identified by its color. Marked areas are either overlaps between incompatible chemisorption sites or unavailable for developing a chemical bond with a depositing molecule. The schematic shows that the available surface diminishes with more nuclei occupying the same surface portion. Examples with (a) two, (b) three, (c) four, and (d) five nuclei.*

same color, through chemisorption. The areas marked with the crosses are either overlaps between incompatible chemisorption sites or unavailable for developing a chemical bond with a depositing molecule. The schematic shows that the available surface decreases with the nuclei density increment - and then with a larger perimeter - occupying the same surface portion, i.e., for high nuclei density. Examples with (a) two, (b) three, (c) four, and (d) five nuclei are shown in the figure. The available space for chemisorption of the DPP molecules on the Si surface then depends on the nuclei surface density. The transient molecules' physisorbed state during the deposition from the concentrated solutions then has an impact on the sheet resistance through the capture zone role: at high solution concentrations, and thus, high nucleation rates, the surface areas available for chemisorption are reduced and, as a consequence, the sheet resistance of the cleaned samples increases. The density of molecules in the solution and arriving on the Si surface has an impact on the bonding mechanisms, changing the local minimum energy configuration, as predicted in our previous work: the most stable energy configuration has a minimum for the covalent bond, but an unstable Van der Walls bond can be formed too [109, 102]. In this frame, the apparent discrepancy between the morphological and electrical data is explained: when the nucleation rate is high, i.e., for high concentrations, the physisorption is more favored than the chemisorption, and the molecules are rinsed away through the chemical treatment. And this happens consistently for all the deposition times, although a complete monolayer is expected to be reached at different times for the different dilutions. When the coverage reaches a level where the spatial distribution plays a role (around 80% and above), the perimeter of the formed nuclei is high, and the capture zone plays a role in impeding/retarding the covalent bonding mechanism. This leads to a decrease in the chemisorption nucleation rate at high concentrations and a corresponding reduction in the electrical efficiency. Together with a scientific understanding, these results allow for better tuning of the doping process and a surface functionalization controlled at nm sizes, which is vital for the applications, specifically for device scaling.

5.5 Conclusions

We investigated the changes caused by different conditions in the DPP deposition mechanisms on Si during the MD process by changing the solution concentration. The morphological data show that: (i) the molecule is deposited on the samples at different rates, higher solution concentrations lead to a faster rise in the sample surface coverage; (ii) nucleation rate shows the same behavior, as it is higher with increasing solution concentrations. Despite the higher deposition rate, the hierarchy of the sheet resistance of the cleaned samples at any given time is inverted with respect to the surface coverage: higher solution concentrations are associated with higher resistances. This behavior has been linked to the ratio of physisorbed vs. chemisorbed molecules present on the samples before the applied surface cleaning. By fitting the Avrami function onto the surface coverage data, the values of n have been calculated, which suggests that the solution concentration influences the dynamics of the DPP deposition. These values of n are associated with the presence of a transient, physisorbed state of the molecules during deposition by using more concentrated deposition solutions. An explanation of the Rs behavior has been proposed. The available space for chemisorption of the DPP molecules on the Si surface depends on the nuclei surface density at any given time. With a higher nucleation rate (and thus, higher solution concentrations), the surface areas available for chemisorption are reduced, and, as a consequence, the sheet resistance of the cleaned samples increases. These results will give a better insight into solution-based molecular deposition processes, as well as allow for a better understanding of the MD process, as well as other technological processes based on molecule-surface interactions like molecular electronics and molecular contact doping, especially for nano-architectures, hollow structures and devices based on nanoscale doped structures. A future work foresees the investigation of the role of the molecule's chemical and physical properties (molecular structure, steric footprint, etc.), substrate orientation, and - when applied to high-density nanostructures - their surface density.

Chapter 6

MD for Silicon Carbide

6.1 Introduction on Silicon Carbide doping

Silicon Carbide (SiC) is a semiconductor with excellent physical, chemical and electronic properties. With its wide band gap, high thermal conductivity, high chemical stability and critical electric field is especially suited for the fabrication of devices with superior characteristics with respect to the current silicon industry standard [124, 125, 126]. Among these advantages, SiC devices can also be operated at high temperature [127]. The SiC crystal exists in several crystalline structures called polytypes, each with a different arrangement of Si and C atoms within its lattice. Each polytype electrical and optical properties is different. For example, 3C-SiC (cubic lattice) has the lowest band gap (2.3 eV) and the highest electron mobility, while 6H-SiC is composed of two-thirds cubic bonds and one-third hexagonal bonds and has larger bandgap (3 eV). The 4H-SiC polytype is known for its large bandgap (3.2 eV), its high electron mobility along the crystal axes and has been extensively used for power electronics applications in the last decades [128]. One of the main characteristics of the doping in SiC is the reduced diffusion coefficients of dopant impurities with respect to the Si counterpart. This is both an advantage and an issue: on one hand, once the incorporation of dopants is achieved, the strong Si-C bonds don’t allow the further diffusion of dopants even at high operation temperature, while on the other hand, the incorporation of dopants itself is hindered by the high temperatures needed in order to observe the dopant diffusion and activation through the SiC crystal. A graph of common dopant diffusion coefficients in SiC can be seen in figure 6.1.

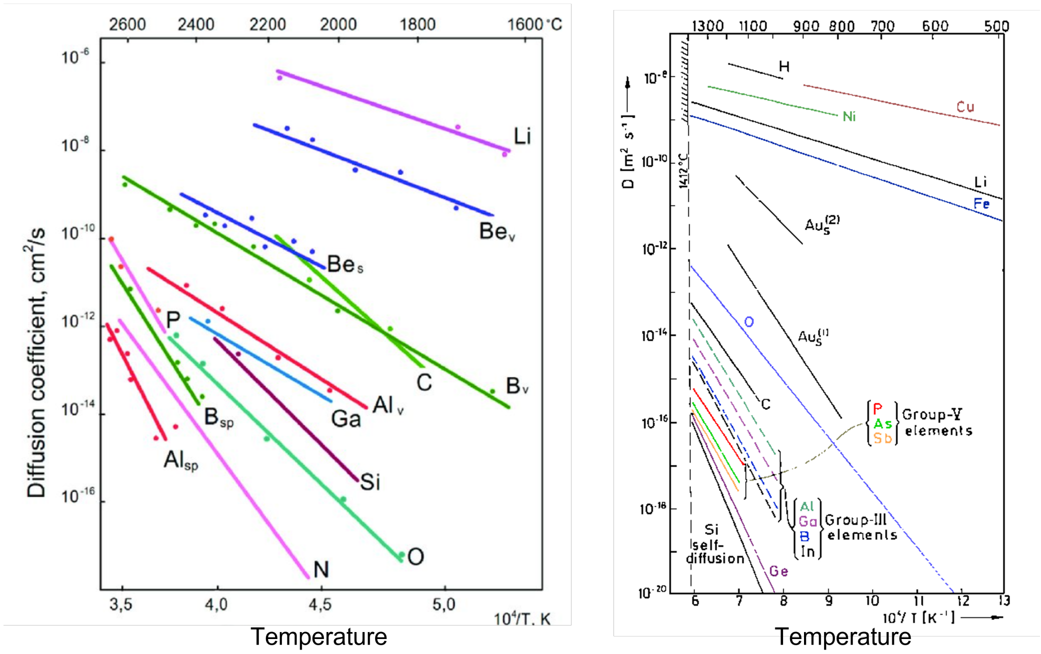

(a) (b)

Figure 6.1: *(a) Diffusion coefficients of dopant species in SiC over temperature. To observe the impurity diffusion in SiC, high temperatures must be reached [129]. P diffusion coefficient is shown in pink; (b) Diffusion coefficients of dopant species in Si over temperature. Diffusion coefficients are orders of magnitude higher than in SiC at lower temperatures [130]. P diffusion coefficient is shown in red.*

For example, in order to achieve the diffusion of phosphorus - shown as a pink line in figure 6.1 - the temperature of at least 2000°C must be reached and, even at these high temperatures, it is still orders of magnitude lower than the phosphorus diffusion coefficient in Si at 1000°C [131]. Since impurity diffusion is heavily reduced in SiC crystals, the most used doping method in order to achieve acceptable levels of incorporation is ion implantation. Although it has been already demonstrated as a valid choice to fabricate simple devices and p-n junctions, some open issues are still to be solved: the high temperature needed for the dopant activation [129], partial activation of high-dose implantation regions [132], incomplete ionization of Aluminum dopants at room temperature [133, 134] and, most of all, the crystal lattice damage induced by the implantation and the difficulties in regenerating defects [135]. The last aspect is especially important because SiC nanoarchitectures have already shown the potentiality to be exploited in many different fields of science and technology [136]: bio-imaging, chemotherapy, photocatalysis, gas sensing and more. Since ion implantation doping can not be achieved without damaging the doped species and since, as already mentioned, damage is hardly recovered in SiC structures, it is especially unsuited for the doping of high surface-to-volume ratio SiC nanostructures. The application of the MD to SiC would allow the ex-situ, conformal doping of nanostructures and may open many possibilities in the field of SiC device fabrication. For this reason, in this thesis, the possibility to apply MD to SiC has been explored, starting with a preliminary study on the possible approaches.

6.2 MD on SiC: feasibility study

As introduced in chapter 2, the fundamental steps of the MD process are (i) the formation of the precursor molecule SAM and (ii) the thermal process needed for the dopant diffusion. To apply the MD to a new substrate, both of these aspects must be studied and adapted to the new system.

The choice of the precursor molecule is paramount in order to meet the needs of point (i). Indeed, the formation of molecular SAMs has been demonstrated in 3C-, 4H-, 6H- and other SiC polytypes by using organophosphonate, silane and organic molecules [137, 138, 139]. For example, the DPP molecule, as well as other organophosphonate compounds, is both a molecule containing a dopant atom for SiC (phosphorus) and capable of self-assembly on the SiC surface.

The requirements of point (ii), as mentioned in the previous section, include a very high temperature thermal process, depending on the diffusing dopant species. As an example, to observe the diffusion of phosphorus in SiC, temperatures between 1800 and 2000 °C must be reached (figure 6.1). The extremely high temperatures could be challenging in the MD process because the deposited precursor molecules could evaporate before being able to release the dopant atom into the substrate. In addition, an eventual SiO_2 capping layer would be exposed to temperatures well above its fusion temperature (1710°C). To tackle this issue, the low-temperature SiC doping approach, found in the work of C. Tin et al. [140], could be integrated into the MD process. The general concept of the approach is to induce the out-diffusion of silicon atoms from the SiC crystal in order to create vacancies into the substrate that, in turn, facilitate the in-diffusion of phosphorus at low temperatures. The creation of vacancies can be obtained by oxidation or silicidation processes. The oxidation-assisted doped samples were fabricated by spinning and curing a layer of silicon-free spin-on phosphorus dopant source on top of the SiC sample. In these conditions, the diffusion of phosphorus was obtained by annealing the samples at 1200-1400°C in O_2 for 1 hour. The silicidation-assisted doped samples were fabricated by depositing and curing the same phos-

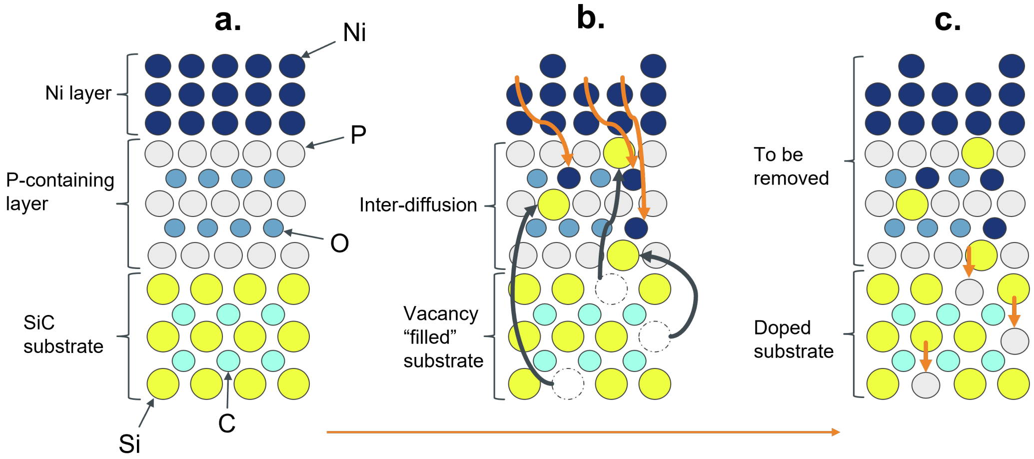

Figure 6.2: *Schematization of the vacancies creation and dopant diffusion in the silicidation-assisted doping. (a) The phosphorus spin-on dopant and the Ni layer are deposited on the SiC sample; (b) the annealing causes the creation of Si-vacancies in the substrate; (c) The presence of Si-vacancies facilitates P diffusion in the SiC lattice.*

phorus spin-on dopant layer on the SiC surface and adding a thin Ni layer on top of it. The annealing step was carried out at 900°C in Ar gas for 1 hour. A schematization of this process can be found in figure 6.2. In both cases, the diffusion profiles were evaluated by Rutherford Backscattering Spectroscopy and Secondary Ion Mass Spectroscopy, revealing the presence of P atoms as deep as 100 nm for the oxidation-assisted case and 300 nm for the silicidation-assisted one, with a concentration peak over $10^{19} cm^{-3}$. By combining the silicidation approach with the conformal properties of the MD technique, the conformal doping of SiC nanostructures at low temperatures could be achieved. For this reason, the study of the Ni and Si behaviour during the MD process was carried out, and it will be presented in the next section.

6.3 Studies of MD on Si-SiO$_2$-Ni systems

6.3.1 Preliminary investigation on DPP on Si effects

The study of the effects of the DPP molecule on the Si surface were conducted in order to understand how the Si surface properties might change during the MD annealing process, after molecule deposition. The substrates were 1-10 ohm/sq p-type <111> Si samples cut into 1x1 cm^2 squares. The molecule deposition was performed after the substrates sonication in acetone, alcohol, and milli-Q water for 5 minutes each, then cleaned in HF for 1 minute. The deposition step has been carried out in 20% concentrated (v/v) solutions of DPP (Abcr, 95%) and mesitylene (Abcr, 98%+) for 150 minutes and kept at the solution's boiling point temperature for the entire time. The thermal diffusion process was performed in N$_2$ environment. Samples were brought to 900°C for 500 s, starting from 600°C, with an initial ramp of 10°C per minute. After the thermal process, the samples were analyzed by Transmission Electron Microscopy (TEM) and Electron Energy Loss Spectroscopy (EELS) in order to evaluate the morphological results of the process. Cross-sectional TEM samples were prepared out of the doped substrates as explained in appendix D. Figure 6.3a shows the TEM image of the sample profile in which the formation of a 2 nm amorphous layer on top of the sub-

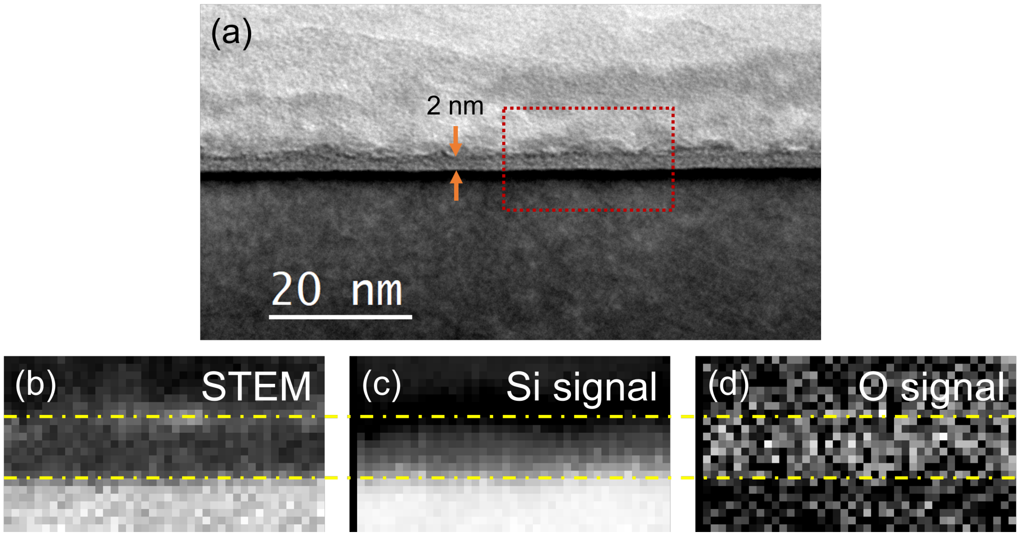

Figure 6.3: *(a) TEM image of the DPP-doped Si substrate after the MD thermal diffusion process; (b) STEM image of the area highlighted by the red dotted line; (c) Si and (d) O signals of the EELS map of the same area. The yellow dashed line indicate the 2 nm layer, composed by Si and O atoms.*

strate can be seen. Figure 6.3b, c and d show the STEM image of the area highlighted in red, and the EELS Si and O signals, respectively.

The comparison between the two EELS signals allows for the recognition of the composition of the 2 nm layer, indicated by the two yellow dashed lines. By recalling the simulations of the DPP-Si interface in figure 4.4, it can be speculated that, during the P diffusion, the decomposition of the molecule leaves the O atoms available for the formation of the SiO_2 layer on the substrate surface.

6.3.2 Effects of the Ni top layer during the DPP-MD process

After the evaluation of the effects of the MD process on the Si surface, the influence of the Ni layer on the system has been investigated. In literature, Ni is known to form several complexes when diffusing within the Si substrate [141]. In order to avoid the formation of nickel silicides that would hinder the doping results during the MD process, we used a barrier layer between the Ni layer and the Si surface. Since the SiO$_2$ layer is used as a barrier layer in many semiconductor processes, we explored the use of this material in our experiments Sample preparation started with the same procedure described in the previous section (6.3.1). After DPP deposition on the Si samples, a 200nm-thick Ni layer has been deposited on them by sputtering. Samples were then annealed at 900°C for 500 s, starting from 600°C, with an initial ramp of 10°C per minute and were analyzed by TEM and EELS.

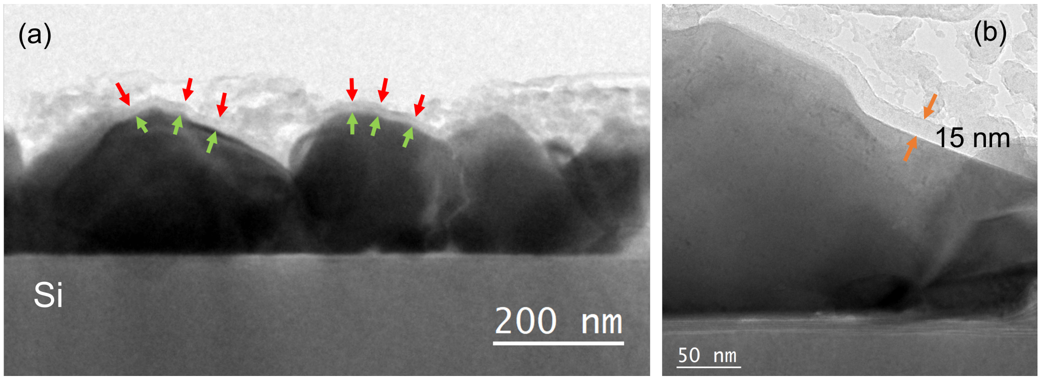

Figure 6.4: *(a) Cross section TEM image of the samples: the image shows the clusterization of the Ni layer and the formation of an overlayer on top of it, indicated by the coloured arrows. (b) Detail of a surface cluster with a 15nm-thick overlayer on the top.*

The cross section TEM image of the samples are shown in figure 6.4a. As it can be seen the Ni layer formed clusters on top of the samples and the Si layer remained uniform. The coloured arrows indicate a thin layer on top of the clusters, following their shape. Figure 6.4b shows a detail of a surface cluster, onto which the overlayer can be clearly distinguished, with a uniform thickness of 15 nm. Again, the EELS analysis, will give information about the distribution profiles of the atom species.

Figure 6.5a shows the STEM detailed image of a surface cluster with the visible overlayer indicated by the coloured arrows. The area surveyed by the EELS is highlighted within the dotted red line. Figure 6.5b, c, d and e contain the detail of the surveyed area and the Si, Ni ad O signal within the surveyed area, respectively. By the EELS signal spectrum

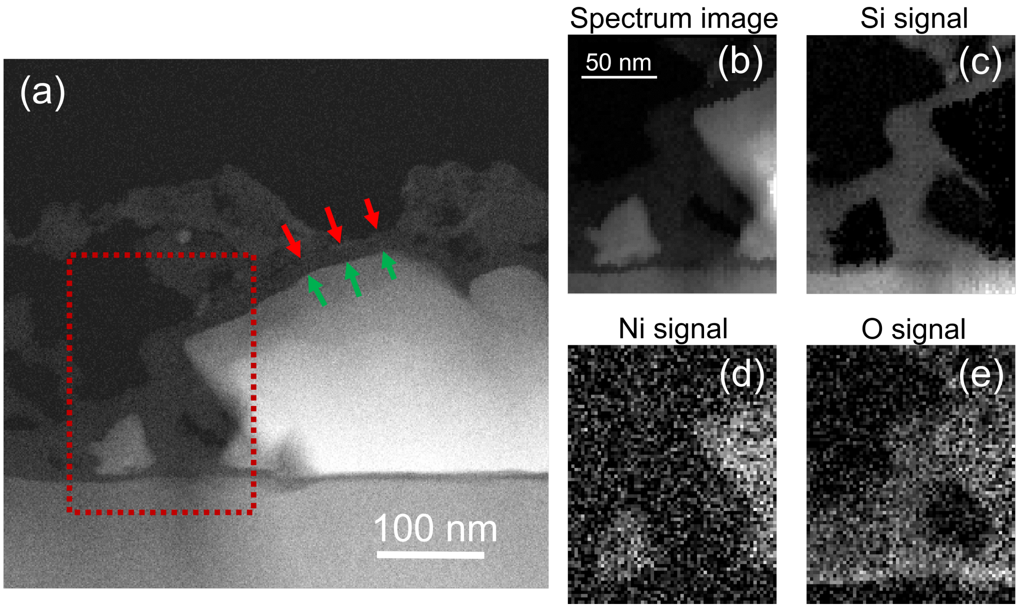

Figure 6.5: *(a) Cross sectional STEM image of a surface cluster. The overlayer is underlined by the coloured arrows. (b) EELS full-spectrum image of the highlighted area within the red dotted line. (c) Si signal, (d) Ni signal and (e) O signal of the collected EELS spectrum in the same area.*

images, it can be deduced that while the Ni and Si signal are confined, respectively, within and outside the shapes of the surface clusters, the O signal is not. As a matter of fact, the Si signal is generated both by the Si substrate and the space within the clusters, while the O signal is generated by the surface layers of the Si substrate, the clusters area and the space between them. From these chemical analysis coupled in situ to the morphological data it can be speculated that, during the annealing process, (i) there's been outdiffusion of silicon from the substrate through the Ni layer towards the surface of the stacked layers, (ii) the Ni layer has undergone clusterization and oxidation and (iii) the O atoms contained in the DPP molecular layer have contributed to the oxidation of the Si surface, the Ni layer and the outdiffused Si. Although this is an ongoing preliminary experiment, it already shows the potential of the Ni layer to stimulate the outdiffusion of Si in the MD process. Future continuation to this investigation will be:

- The removal of the top cluster layer and the evaluation of the electrical and chemical properties of the remaining Si substrate;
- he process characterization in terms of Ni layer thickness and annealing parameters such as temperature, ambient and time;
- The deposition of a SiO_2 layer before the Ni sputtering as an additional barrier between the Si surface and the Ni layer;
- The continuation of the feasibility study with the application of numerical methods to simulate the Si outdiffusion behaviour.

Conclusions

The research activity of this thesis has been focused on the study of the innovative conformal doping technique called Molecular Doping.

The first part of this work has been focused on the study of the molecule layers formation on top of the sample after the MD molecule deposition step. The investigation involved the morphological evaluation of the samples at several stages of the deposition process through SEM analysis. The surface coverage data shows that the molecules self assemble into a full monolayer after 100-120 minutes of deposition and that after the formation of the first layer, a second layer of molecules starts to form on top of it. By treating the samples with a surface cleaning process, the surface coverage drops, especially at prolonged deposition times. This indicates that the first layer of DPP molecules develop mostly chemical, thus strong, bonds with the Si surface while the molecules of the second layer are attached by physical forces to the first. To corroborate these results, DFT calculations of the system have been made. The simulations show that the first layer molecules bond through P-O-Si chains to the substrate and through P-0-P chains among themselves. Moreover, the DFT confirms the weak nature of the forces between the second and first layer of the DPP. The electrical measurements, made by the SRP technique, demonstrate the efficacy of the MD process in both the cleaned and the as-deposited cases, with a higher dopant dose, dopant concentration peak and junction depth in the case of the as-deposited samples, demonstrating the role of physisorbed molecules in the MD deposition step.

The successive experiments are presented in the second part of the thesis and were focused on the deposition mechanism changes caused by the DPP concentration in the deposition solution. Again, the morphological data were extracted by the SEM analysis. The results show that the solution concentration influences both the rate of deposition and the rate of nucleation. Both rates are higher with increasing deposition solution concentrations. The electrical measurements of the cleaned samples sheet resistance show us an inverted hierarchy instead: higher resistances are associated with the higher solution concentration samples. This aspect can be linked to the nature of the physisorbed vs chemisorbed molecules at the end of the deposition process, right before the application of the surface cleaning. As a matter of fact, by fitting the surface coverage data with the Avrami function, the values of the exponent n have been calculated for each sample series. These values are associated with the presence of a transient, physisorbed state of the molecules, which is more present with he use of higher concentrated deposition solutions. By combining these results, it can be deduced that the surface concentration influences the dynamics of the DPP deposition. An explanation of the behaviour of the cleaned samples sheet resistance can also be proposed based on the morphological nucleation data. The available sites for chemisorption of the DPP molecule on Si depend on the fraction of uncovered surface. With higher deposition solution concentration, a higher nucleation rate has been measured and thus the chemisorption-available sites are reduced. As a consequence, the sheet resistance of the cleaned samples has a reversed hierarchy with respect to the presented surface coverage data.

These investigations on the DPP-Si system and MD process will add to the comprehension of how the DPP molecule interacts with the Si surface during the MD deposition process and, with this understanding, will give insights into solution-based molecular deposition processes as well as other technological applications based on molecule-surface interactions.

In the third part of the thesis, the feasibility study for the application of the MD process in SiC substrate has been presented. Among the aspects to be studied, the possibility of reducing the thermal budget for the diffusion of dopants in the SiC lattice has been presented. The approach is based on the interaction between a thin Ni layer with the SOD phosphorus dopant on SiC complex, which causes the outdiffusion of Si from the SiC lattice. In order to evaluate the possibility of incorporating this approach into the MD process, Si samples have been prepared by including the deposition of a Ni layer on top of the DPP molecule layer after the MD deposition step. The samples have been examined by TEM and EELS, which show (i) the formation of a SiO_2 layer on the Si surface, (ii) the clusterization of the Ni layer, (iii) the oxidation of the Ni layer and (iv) the formation of a SiO_2 overlayer on top of the surface clusters. These results show that the presence of the Ni layer stimulated the outdiffusion of Si from its lattice, and that the formation of the SiO_2 layer is capable of preventing the formation of Ni-Si complexes in the substrate. This is a preliminary study and further investigation on the introduction of Ni into the DPP-MD process will allow both further understanding of the MD in Si and the possibility of applying the MD to SiC substrates and nanostructures.

Appendix A

Spreading Resistance Profiling

Spreading Resistance Profiling is a Two-Point Probe system for the measurements that provides resistivity vs depth profiles of samples, which is used for the extrapolation of the dopant profile in semiconductors. The two probes are lowered on a previously beveled sample with a 50mum spacing between them. Additional sample surface preparation can be implemented to improve the probe-surface contact. The application of a known current between the electrodes, and the measurement of the voltage drop between the probes, allows for the measurement of the resistance.

The spreading resistance profile is obtained by moving the two probes along the bevel and to make a series of I-V measurements as shown in figure A.1. The profile depth is adjusted as the probes move by a factor depending on the bevel angle. Resistance measurements are then converted to carrier concentration levels by the use of calibration curves. Information on the dopant dose can also be extrapolated by the integration of the depth profiles.

In this thesis, SRP measurements have been collected with a SSM150 tool. They have been used to analyze the carrier concentration profile of doped samples. The samples have been prepared with a low bevel angle in order to achieve high accuracy of the measurements depth and resolutions of about 3 nm have been achieved.

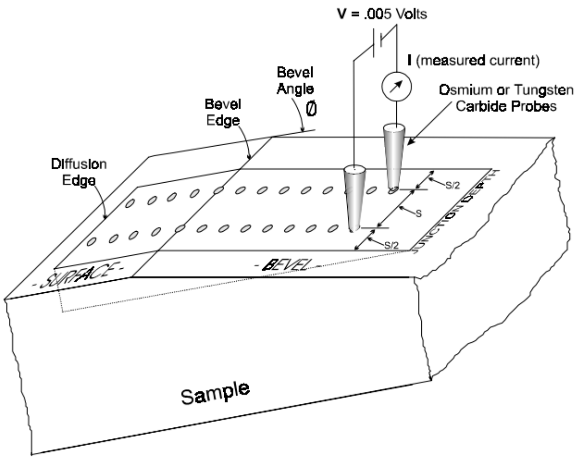

Figure A.1: Spreading Resistance Profiling measurements on a beveled sample.

Appendix B

Four-Point Probe

The Four-Point Probe characterization is used to determine the sheet resistivity of a homogeneous layer, which can be represented by the following equation:

$$\rho_S = \frac{\rho}{t} \tag{B.1}$$

With t being the thickness of the layer to be electrically evaluated. In the case of semiconductor p-n juctions, the thickness t is equal to the junction depth. The four probes are arranged in a line as shown in figure B.1.

Usually, the two outer probes are used to carry the current while the two inner probes are used to measure the voltage drop between them. The choice of the probe distances influences the results of the measurement. If the spacings between the probes are equal, sheet resistivity can be expressed as follows:

$$\rho_S = (\frac{\pi}{\ln 2})R_a \approx 4.532R_a \tag{B.2}$$

Where R_a is the resistance value obtained by reversing the polarity of the current. The measurements are affected by the probe and the sample geometry effects, which can be minimized by (i) maximizing the average distance of the probes from the edges of the sample and (ii) applying a correction factor based on the sample shape and surface area.

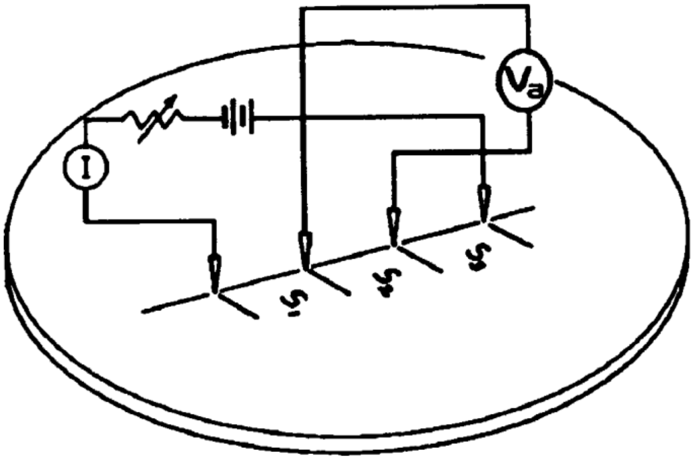

Figure B.1: Conventional configuration of the four-point probe measurement system.

In this thesis, the 4PP measurements have been employed to evaluate the electrical properties of doped samples. Samples have been cut to 1x1 cm^2 squares in order to standardize the size and geometry among the various samples examined. I-V characteristics have been collected with a Keithley 237 source-measure unit. Measurements were done in a dark environment to eliminate light-induced conductivity modifications on the samples.

Appendix C

Scanning Electron Microscopy

Conventional optical microscopy is capable of a magnification of 1000x by using photons as probes for the samples investigation. Scanning Electron Microscopy (SEM) uses electrons instead, which can be accelerated to high energies (usually between 2 and 1000 keV) in order to poduce a small wavelength beam with a higher resolution. Electron wavelengths are usually contained within 0.027 and 0.0009 nm. A schematic of SEM parts can be found in figure C.1.

After the electrons are emitted from the electron gun, on top, they pass through three sets of electromagnetic lenses before reaching the sample: the condenser lenses, the deflection coil and the final lens. The condenser lenses purpose is to collimate the beam in order to make it as narrow as possible. After collimation, the electron beam passes through the deflection coils, which bend the beam in order to direct it towards a specific spot of the sample. The last beam adjustments are made by a system of final lenses. The electrons then interact with the sample surface which, in turn, will respond to the interaction with secondary electrons, photons and so on. These particles are collected by detectors, either electron or photon detectors, they are converted into electrical signals and, with the aid of an amplifier, transmitted to an electronic interface. The electron beam is directed towards subsequent spots and the image is built pixel-by-pixel, hence the 'scanning' characteristic of the technique.

There are many possible interaction between the electron beam and the sample to be analyzed: low-angle and high-angle scattering, emission

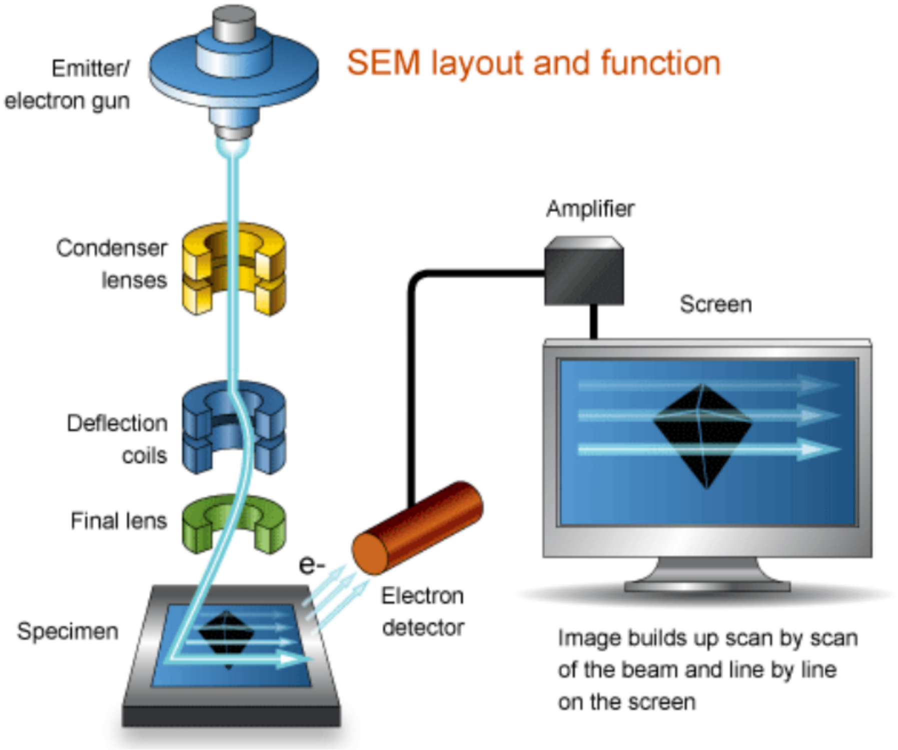

Figure C.1: *Scanning Electron Microscope schematics.*

of a secondary electron, characteristic x-ray emission and Auger electron emission. Each one of these interactions products can give information about the observed sample: by combining these signals, details about morphology, chemical composition and electrical behaviour of sample surfaces can be provided.

1. *Secondary electrons (SE)*: These electrons are those that escape from the sample surface at low energy ($\approx 50eV$). These provide a signal with very high spatial resolution since they come from the shallower parts of the surface, usually by a depth comparable to the size of the electron probe. They primarily give morphological information although contrast is also slighty influenced by the atomic number of the probed zones.

2. *BackScattered Electrons (BSE)*: Backscattered electrons are the incident ones that are scattered through a larger angle and re-emerge from the surface. They have a much higher energy than te SE, and can give information wiht a lower resolution, since they interact with a deeper part of the surface. They give mostly compositional information, since elements with a higher atomic number also give a higher contrast. Some crystallographic information can be deduced too by the analysis of electron channeling through crystal planes.

3. *Electron Beam Induced Current (EBIC)*: The electron interaction usually produces many electron-hole pairs which then recombine almost instantly. If an electric field is applied on the sample, the electron-hole pair will not recombine and the induced current can be measured. This current gives information about the conductivity of the sample, the lifetime of charge carriers inside the material and their mobilities. It is often used to determine electrically active defect maps of semiconductor surfaces.

4. *Cathodoluminescence (CL)*: The recombination of induced electron-hole pairs generates photons. Their wavelength depends on the characteristics of the explored surface (semiconductor bandgap, composition, etc.). The addition of specifc detectors must be accomplished before a SEM setup can evaluate this kind of signal. Resolutions are not optimal, but still under the microns domain.

5. *Voltage-contrast imaging*: By applying a voltage across the semiconductor, the interaction of the electron beam with the surface is modified and a higher number of secondary electrons can be collected. This technique is often used in circuit failure analysis by comparing images of the

circuit without and with applied voltage across each region of the device.

6. *Auger electrons and x-rays*: Auger electrons give information about the chemistry of the surface. The energies at which they are generated are atom-specific and, by the evaluation of these energy, the species contained in the probed beam-spot and their surroundings can be recognized. Emitted x-rays give information about the electronic states of the electron shells of atoms and, thus, can be interpreted to understand details about the nature of the surface sample species. They are usually collected by an Energy Dispersive X-ray spectroscope (EDX). By using calibration curves, limited quantitative information can be also obtained.

In this thesis, SEM is used to evaluate the presence, the morphology and the evolution of precursor-molecule SAMs on Si <111> samples. The data were collected by employing a Field Emission Gun (FEG-SEM). The FEG, also known as 'cold cathode' emitter, provide the brightest beam among the available electron guns while maintaining very small deviations in the electron beam energy. This is accomplished by the use of finely tuned high electrical fields to the gun tip, until the quantum tunneling of electrons towards the free state occurs. In order to preserve the tip, the vacuum level requirement for the use of a FEG is quite high (10^{-10} Torr), which dramatically increases the cost of FEG-SEM microscopes.

Appendix D

Transmission Electron Microscopy

In Transmission Electron Microscopy (TEM) the sample is thinned to a few hundreds of nm at most and is then subjected to a beam of high-energy electrons. The image is then formed by the electron that have passed through the sample, interacting with it. Image contrast depend on three contributes: absorption, diffraction and phase contrast. Absorption contrast depends on the fraction of energy lost by an electron that interacts with a sample atom. The higher the atomic mass of the element, the higher the contrast. This kind of contrast is also influenced by the sample thickness, since the electron transmission is modified by it. An image obtained by absorption contrast is called a "bright-field" image. Diffraction contrast image, or "dark-field" image, is obtained by the signal coming from the electron diffracted by the specimen. If the sample is crystalline, a spot pattern will be obtained depending on the orientation of crystal planes. Phase contrast is obtained by letting more than one electron beam pass through the specimen and is extrated by the interference between these beams. The technique is also known as high-resolution electron microscopy (HREM).

TEM can also be used as a Scanning Transmission Electron Microscope (STEM), in which a high-brightness beam of electron is directed through the specimen by scanning coils in a sub-nm sized spot. The transmitted electrons produce signals that are collected by sensors in order to construct an image in the pixel-by-pixel configuration, similarly to a SEM image.

With the use of the STEM configuration, the Electron Energy Loss Spectroscopy (EELS) spectra can be collected. The technique involves the evaluation of the electron energy loss through specific spots of the sample. The energy loss heavily depends on the targeted atom species and its bonds. This technique enables the determination of chemical composition, electronic band structure, defects and grain boundary maps of the analyzed sample.

Appendix E

Error function

The error function, denoted as *erf(x)*, is a mathematical funcion that finds applications through various branches of science and engineering. It is commonly used in statistics, probability theory and the analysis of Gaussian distributions. It is given by the following expression:

$$erf(x) = (\frac{2}{\sqrt{\pi}}) \int_0^x e^{(-t^2)} dt \tag{E.1}$$

The integral is not expressible in terms of elementary functions and is usually computed through numerical methods. The error function is widely used in Probability theory and Statistics to compute cumulative distribution functions for normal distributions, in Signal Processing, to analyze digital modulation schemes in communications systems, in Mathematical Analysis to solve integral and partial differential equations and in Physics, as a tool to study diffusion processes and heat conduction phenomena.

In this thesis, it has been included in the study of the atomistic diffusion processes related to the doping of semiconductor materials.

Bibliography

[1] M. Faraday, *Experimental Researches in Electricity* (printers And Publishers To The University Of London, London, Red Lion Court, Fleet Street, 1849), Vol. 1, pp. 122–124.

[2] A H W Il, Proceedings of the Royal Society of London. Series A, Containing Papers of a Mathematical and Physical Character **133**, 458 (1931).

[3] Russell S Ohl, Light-sensitive electric device, 1946, uS Patent 2,402,662.

[4] W. Shockley, Bell System Technical Journal **28**, 435 (1949).

[5] Jack S Kilby, Miniaturized electronic circuits, 1964, uS Patent 3,138,743.

[6] Leo Esaki and Yuriko Miyahara, Solid-State Electronics **1**, 13 (1960).

[7] Gordon Moore, Electronics Magazine **38**, 114 (1965).

[8] Robert H. Dennard, Fritz H. Gaensslen, Hwa Nien Yu, V. Leo Rideout, Ernest Bassous, and Andre R. Leblanc, IEEE Journal of Solid-State Circuits **9**, 256 (1974).

[9] B. Lojek, *History of Semiconductor Engineering* (Springer Science and Business Media, Tiergartenstraße 17, 69121 Heidelberg, Germany, 2007), pp. 321–3.

[10] J. C. Liu, S. Mukhopadhyay, Amit Kundu, S. H. Chen, H. C. Wang, D. S. Huang, J. H. Lee, M. I. Wang, Ryan Lu, S. S. Lin, Y. M. Chen, H. L. Shang, P. W. Wang, H. C. Lin, Geoffrey Yeap, and Jun He, Technical Digest - International Electron Devices Meeting, IEDM **2020-December**, 9.2.1 (2020).

[11] John Shalf, Philosophical Transactions of the Royal Society A **378**, (2020).

[12] Riko Radojcic, More-than-Moore 2.5D and 3D SiP Integration 1 (2017).

[13] Johnny C Ho, Roie Yerushalmi, Zachery A Jacobson, Zhiyong Fan, Robert L Alley, and Ali Javey, Nature Materials **7**, 62 (2008).

[14] S. Streetman, Ben G.; Banerjee, *Solid State electronic Devices 5th ed.* (New Jersey: Prentice Hall, NJ, 2000), pp. 321–3.

[15] M. Shur, *Physics Of Semiconductor Devices* (Prentice-Hall Of India Pvt. Limited, M-97 Connaught Circus, New Delhi, 1998).

[16] J. Wood and Gautam Majumdar, Reference Module in Materials Science and Materials Engineering (2016).

[17] K. L. Choy, Progress in Materials Science **48**, 57 (2003).

[18] Md Momtazur Rahman and Md Nazmul Hasan, International Journal of Thin Films Science and Technology **5**, 45 (2016).

[19] S.M. Sze, *VLSI Technology*, *Electronics and electronic circuits* (McGraw-Hill, New York, 1988).

[20] Mark van Dal, Nadine Collaert, G. Doombos, G. Vellianitis, G. Curatola, B.J. Pawlak, Ray Duffy, C. Jonville, B. Degroote, Efrain Altamirano-Sanchez, E. Kunnen, M. Demand, S. Beckx, T. Vandeweyer, C. Delvaux, Frederik Leys, Andriy Hikavyy, R. Rooyackers, Monja Kaiser, and R.J.P. Lander, in *Highly manufacturable FinFETs with sub-10nm fin width and high aspect ratio fabricated with immersion lithography* (IEEE, Kyoto, Japan, 2007), pp. 110 – 111.

[21] Ray Duffy, Noel Kennedy, Gioele Mirabelli, Emmanuele Galluccio, Paul K Hurley, Justin D Holmes, and Brenda Long, in *2018 18th International Workshop on Junction Technology (IWJT)* (IEEE, Shanghai, China, 2018), pp. 1–6.

[22] Rosaria A Puglisi, Cristina Garozzo, Corrado Bongiorno, Salvatore Di Franco, Markus Italia, Giovanni Mannino, Silvia Scalese, and Antonino La Magna, Solar Energy Materials and Solar Cells **132**, 118 (2015).

[23] Hao Zhu, Nanowires - New Insights (2017).

[24] Giselle Jimenez-Cadena, Jordi Riu, and F Xavier Rius, Analyst **132**, 1083 (2007).

[25] B.R.A. Neves, M.E. Salmon, P.E. Russell, and E.B. Troughton, Langmuir **17**, 8193 (2001).

[26] J G Ekerdt, K J Klabunde, J R Shapley, J M White, and J T Yates, The Journal of Physical Chemistry **92**, 6182 (1988).

[27] Johnny C Ho, Alexandra C Ford, Yu-Lun Chueh, Paul W Leu, Onur Ergen, Kuniharu Takei, Gregory Smith, Prashant Majhi, Joseph Bennett, and Ali Javey, Applied Physics Letters **95**, 72108 (2009).

[28] Joel Barnett, Richard Hill, Wei-Yip Loh, Chris Hobbs, Prashant Majhi, and Raj Jammy, in *2010 International Workshop on Junction Technology Extended Abstracts* (IEEE, Shanghai, China, 2010), pp. 1–4.

[29] Brenda Long, Giuseppe Alessio Verni, John O'Connell, Justin Holmes, Maryam Shayesteh, Dan O'Connell, and Ray Duffy, in *Proceedings of the International Conference on Ion Implantation Technology* (Institute of Electrical and Electronics Engineers Inc., Portland, OR, USA, 2014).

[30] Johnny C Ho, Roie Yerushalmi, Gregory Smith, Prashant Majhi, Joseph Bennett, Jeffri Halim, Vladimir N Faifer, and Ali Javey, Nano Letters **9**, 725 (2009).

[31] Md. Morsaline Billah, Henry C.W. Hays, Christopher S. Hodges, Sreenivasan Ponnambalam, Ravi Vohra, and Paul A. Millner, Sensors and Actuators B: Chemical **173**, 361 (2012).

[32] Robert G. Chapman, Emanuele Ostuni, Lin Yan, and George M. Whitesides, Langmuir **16**, 6927 (2000).

[33] Vivien Lacour, Khalid Moumanis, Walid M Hassen, Céline Elie-Caille, Thérèse Leblois, and Jan J Dubowski, Langmuir **35**, 4415 (2017).

[34] Van-Thao Ta, Satish Balasaheb Nimse, Keum-Soo Song, Junghoon Kim, Danishmalik Rafiq Sayyed, Van-Thuan Nguyen, and Taisun Kim, Chemical Communications **47**, 11261 (2011).

[35] Liang Ye, Sidharam P Pujari, Han Zuilhof, Tibor Kudernac, Michel P de Jong, Wilfred G van der Wiel, and Jurriaan Huskens, ACS Applied Materials & Interfaces **7**, 3231 (2015).

[36] Sebastiano Caccamo and Rosaria Anna Puglisi, Nanomaterials **11**, 2006 (2021).

[37] Rosaria A Puglisi, Sebastiano Caccamo, Luisa D'Urso, Gabriele Fisichella, Filippo Giannazzo, Markus Italia, and Antonino La Magna, physica status solidi (a) **212**, 1685 (2015).

[38] Rosaria A Puglisi, Sebastiano Caccamo, Corrado Bongiorno, Giuseppe Fisicaro, Luigi Genovese, Stefan Goedecker, Giovanni Mannino, and Antonino La Magna, Scientific reports **9**, 1 (2019).

[39] Xuejiao Gao, Bin Guan, Abdelmadjid Mesli, Kaixiang Chen, and Yaping Dan, Nature Communications **9**, 118 (2018).

[40] Janneke Veerbeek, Liang Ye, Wouter Vijselaar, Tibor Kudernac, Wilfred G Van Der Wiel, and Jurriaan Huskens, Nanoscale **9**, 2836 (2017).

[41] Rick Elbersen, Wouter Vijselaar, Roald M. Tiggelaar, Han Gardeniers, and Jurriaan Huskens, Advanced Materials **27**, 6781 (2015).

[42] Jiajing He, Chulin Huang, Huimin Wen, Xiaoming Wang, Yongning He, and Yaping Dan, Nanotechnology **31**, 195201 (2020).

[43] I. Ok, K.-W. Ang, C. Hobbs, R. H. Baek, C. Y. Kang, J. Snow, P. Nunan, S. Nadahara, P. D. Kirsch, and R. Jammy, in *2012 12th International Workshop on Junction Technology* (IEEE, Shanghai, China, 2012), pp. 29–34.

[44] K.-W. Ang, J. Barnett, W.-Y. Loh, J. Huang, B.-G. Min, P. Y. Hung, I. Ok, J. H. Yum, G. Bersuker, M. Rodgers, V. Kaushik, S. Gausepohl, C. Hobbs, P. D. Kirsch, and R. Jammy, in *2011 International Electron Devices Meeting* (IEEE, Washington, DC, USA, 2011), pp. 35.5.1–35.5.4.

[45] Y.-J. Lee, T.-C. Cho, K.-H. Kao, P.-J. Sung, F.-K. Hsueh, P.-C. Huang, C.-T. Wu, S.-H. Hsu, W. H. Huang, H.-C. Chen, Y. Li, M. I. Current, B. Hengstebeck, J. Marino, T. Büyüklimanli, J.-M. Shieh, T.-S. Chao, W.-F. Wu, and W.-K. Yeh, in *2014 IEEE International Electron Devices Meeting* (IEEE, Washington, DC, USA, 2014), pp. 32.7.1–32.7.4.

[46] Cristina Garozzo, Corrado Bongiorno, Salvatore Di Franco, Markus Italia, Antonino La Magna, Silvia Scalese, Paolo Maria Sberna, and Rosaria A. Puglisi, physica status solidi (a) **210**, 1564 (2013).

[47] C. Garozzo, F. Giannazzo, M. Italia, A. La Magna, V. Privitera, and R.A. Puglisi, Materials Science and Engineering: B **178**, 686 (2013), advanced materials and characterization techniques for solar cells.

[48] Josiah Willard Gibbs, *Elementary principles in statistical mechanics: developed with especial reference to the rational foundations of thermodynamics* (C. Scribner's sons, New York City, 1902).

[49] Vladimir G Dubrovskii, *Nucleation theory and growth of nanostructures* (Springer, Heidelberg, 2014).

[50] R. Aveyard and B. Vincent, Progress in Surface Science **8**, 59 (1977).

[51] Jürn WP Schmelzer, Alexander S Abyzov, and Vladimir G Baidakov, International Journal of Applied Glass Science **8**, 48 (2017).

[52] FC Collins, Zeitschrift für Elektrochemie, Berichte der Bunsengesellschaft für physikalische Chemie **59**, 404 (1955).

[53] D Kashchiev, Surface Science **14**, 209 (1969).

[54] Hiromu Wakeshima, The Journal of Chemical Physics **22**, 1614 (1954).

[55] Françoise Rouquerol, Jean Rouquerol, and Kenneth Sing, in *Adsorption by Powders and Porous Solids*, edited by Françoise Rouquerol, Jean Rouquerol, and Kenneth Sing (Academic Press, London, 1999), pp. 1–26.

[56] Milos Toth, Charlene Lobo, Vinzenz Friedli, Aleksandra Szkudlarek, and Ivo Utke, Beilstein Journal of Nanotechnology **6**, 1518 (2015).

[57] P Kisuuk, Journal of Physics and Chemistry of Solids **5**, 78 (1958).

[58] Achim von Keudell, Plasma Sources Science and Technology **9**, 455 (2000).

[59] Isabel Z Jones, Roger A Bennett, and Michael Bowker, Surface science **439**, 235 (1999).

[60] Michael Bowker, Quanmin Guo, and Richard Joyner, Surface science **253**, 33 (1991).

[61] M Kunat, Ch Boas, Th Becker, U Burghaus, and Ch Wöll, Surface science **474**, 114 (2001).

[62] M Bowker, E Rowbotham, FM Leibsle, and S Haq, Surface science **349**, 97 (1996).

[63] TGA Youngs, S Haq, and Michael Bowker, Surface Science **602**, 1775 (2008).

[64] Niklas Nilius, Surface Science Reports **64**, 595 (2009).

[65] U Burghaus, Surface Review and Letters **10**, 7 (2003).

[66] Albert Frederick Carley, Philip Rosser Davies, and Meirion Wyn Roberts, Philosophical Transactions of the Royal Society A: Mathematical, Physical and Engineering Sciences **363**, 829 (2005).

[67] Michael Bowker, Matthew House, Abdulmohsen Alshehri, Catherine Brookes, Emma K Gibson, and Peter P Wells, Catalysis, Structure & Reactivity **1**, 95 (2015).

[68] Brian Cantor, *The Equations of Materials* (Oxford University Press, Oxford, 2020).

[69] Michael C. Weinberg, Dunbar P. Birnie, and Vitaly A. Shneidman, Journal of Non-Crystalline Solids **219**, 89 (1997), glass Crystallization.

[70] Cecilia Herrero, Camille Scalliet, MD Ediger, and Ludovic Berthier, arXiv preprint arXiv:2210.04775 (2022).

[71] Janusz Lelito, Materials **13**, 2815 (2020).

[72] Mehdi Malekan and Reza Rashidi, Applied Physics A **127**, 1 (2021).

[73] I Sinha and RK Mandal, Journal of Non-Crystalline Solids **357**, 919 (2011).

[74] Stoyan Budurov, Tony Spassov, and Krassimir Marchev, Journal of materials science **22**, 3485 (1987).

[75] H.-Y. Nie, M J Walzak, and N S McIntyre, Langmuir **18**, 2955 (2002).

[76] Irina Gouzman, Manish Dubey, Michael D Carolus, Jeffrey Schwartz, and Steven L Bernasek, Surface Science **600**, 773 (2006).

[77] R A Puglisi, G Nicotra, S Lombardo, C Spinella, G Ammendola, and C Gerardi, Phys. Rev. B **71**, 125322 (2005).

[78] Pablo Ordejón, Emilio Artacho, and José M. Soler, Physical Review B **53**, R10441 (1996).

[79] John P. Perdew, Kieron Burke, and Matthias Ernzerhof, Physical Review Letters **77**, 3865 (1996).

[80] Hendrik J. Monkhorst and James D. Pack, Physical Review B **13**, 5188 (1976).

[81] Noel Kennedy, Shane Garvey, Barbara MacCioni, Luke Eaton, Michael Nolan, Ray Duffy, Fintan Meaney, Mary Kennedy, Justin D. Holmes, and Brenda Long, Langmuir **36**, 9993 (2020).

[82] Daniel K. Schwartz, Annual Review of Physical Chemistry **52**, 107 (2001).

[83] Walter Hayduk and Harry Laudie, AIChE Journal **20**, 611 (1974).

[84] Pablo Jensen, Pierre Deltour, Laurent Bardotti, and Jean-Louis Barrat, *Surface Diffusion* (Springer US, Boston, MA, 1997), pp. 403–408.

[85] Raquel Moiraghi, Ariel Lozano, Eric Peterson, Arthur Utz, Wei Dong, and H. Fabio Busnengo, Journal of Physical Chemistry Letters **11**, 2211 (2020).

[86] K. N. (King-Ning) Tu, *Electronic thin film science : for electrical engineers and materials scientists* (Macmillan, New York, 1992 - 1992).

[87] Ruowei Yi, Yayun Mao, Yanbin Shen, and Liwei Chen, Journal of the American Chemical Society **143**, 12897 (2021).

[88] Sergio A Paniagua, Anthony J Giordano, O'Neil L Smith, Stephen Barlow, Hong Li, Neal R Armstrong, Jeanne E Pemberton, Jean-Luc Bredas, David Ginger, and Seth R Marder, Chemical reviews **116**, 7117 (2016).

[89] Abraham Ulman, *An Introduction to Ultrathin Organic Films: From Langmuir–Blodgett to Self–Assembly* (Academic press, San Diego, 2013).

[90] Frank Schreiber, Journal of Physics: Condensed Matter **16**, R881 (2004).

[91] IH Campbell, JD Kress, RL Martin, DL Smith, NN Barashkov, and JP Ferraris, Applied Physics Letters **71**, 3528 (1997).

[92] Slawomir Braun, William R Salaneck, and Mats Fahlman, Advanced materials **21**, 1450 (2009).

[93] Chad A Mirkin and Mark A Ratner, Annual Review of Physical Chemistry **43**, 719 (1992).

[94] C Garozzo, F Giannazzo, M Italia, A La Magna, V Privitera, and R A Puglisi, Materials Science and Engineering: B **178**, 686 (2013).

[95] Chul Jin Park, Sang Min Jung, Jin Hwan Kim, and Moo Whan Shin, Semiconductor Science and Technology **35**, 055028 (2020).

[96] Rosaria A. Puglisi, Sebastiano Caccamo, Corrado Bongiorno, Giuseppe Fisicaro, Luigi Genovese, Stefan Goedecker, Giovanni Mannino, and Antonino La Magna, Scientific Reports **9**, 1 (2019).

[97] Johnny C Ho, Roie Yerushalmi, Gregory Smith, Prashant Majhi, Joseph Bennett, Jeffri Halim, Vladimir N Faifer, and Ali Javey, Nano Letters **9**, 725 (2009).

[98] W Pim Voorthuijzen, M Deniz Yilmaz, Wouter J M Naber, Jurriaan Huskens, and Wilfred G van der Wiel, Advanced Materials **23**, 1346 (2011).

[99] Rosaria A Puglisi, Cristina Garozzo, Corrado Bongiorno, Salvatore Di Franco, Markus Italia, Giovanni Mannino, Silvia Scalese, and Antonino La Magna, Solar Energy Materials and Solar Cells **132**, 118 (2015).

[100] Sebastiano Caccamo and Rosaria Anna Puglisi, Nanomaterials **11**, (2021).

[101] Avra Tzaguy, Prajith Karadan, Krushnamurty Killi, Ori Hazut, Iddo Amit, Yossi Rosenwaks, and Roie Yerushalmi, Advanced Materials Interfaces **7**, 1902198 (2020).

[102] Mattia Pizzone, Maria Grazia Grimaldi, Antonino La Magna, Neda Rahmani, Silvia Scalese, Jost Adam, and Rosaria A. Puglisi, Nanomaterials **11**, (2021).

[103] Liang Ye, Sidharam P Pujari, Han Zuilhof, Tibor Kudernac, Michel P de Jong, Wilfred G van der Wiel, and Jurriaan Huskens, ACS Applied Materials & Interfaces **7**, 3231 (2015).

[104] A Eberhardt, P Fenter, and P Eisenberger, Surface Science **397**, L285 (1998).

[105] Ivo Doudevski, William A Hayes, and Daniel K Schwartz, Phys. Rev. Lett. **81**, 4927 (1998).

[106] Scott Holmes, Richard E. Palmer, and Quanmin Guo, The Journal of Physical Chemistry C **123**, 24104 (2019).

[107] Daniel K Schwartz, Annual review of physical chemistry **52**, 107 (2001).

[108] Ramūnas Valiokas, Goran Klenkar, Ali Tinazli, Annett Reichel, Robert Tampé, Jacob Piehler, and Bo Liedberg, Langmuir **24**, 4959 (2008).

[109] John P Folkers, Paul E Laibinis, George M Whitesides, and John Deutch, The Journal of Physical Chemistry **98**, 563 (1994).

[110] Ryo Yamada, Hiromi Wano, and Kohei Uosaki, Langmuir **16**, 5523 (2000).

[111] Atul N Parikh, David L Allara, Issam Ben Azouz, and Francis Rondelez, The Journal of Physical Chemistry **98**, 7577 (1994).

[112] Melvin Avrami, The Journal of Chemical Physics **7**, 1103 (1939).

[113] Melvin Avrami, The Journal of Chemical Physics **8**, 212 (1940).

[114] Melvin Avrami, The Journal of Chemical Physics **9**, 177 (1941).

[115] YP Khanna and TJ Taylor, Polymer Engineering & Science **28**, 1042 (1988).

[116] Alberto Pimpinelli, Levent Tumbek, and Adolf Winkler, The Journal of Physical Chemistry Letters **5**, 995 (2014).

[117] PA Mulheran and JA Blackman, Physical review B **53**, 10261 (1996).

[118] Martin Körner, Mario Einax, and Philipp Maass, Physical Review B **86**, 085403 (2012).

[119] Artem Shelemin, Pavel Pleskunov, Jaroslav Kousal, Jonas Drewes, Jan Hanuš, Suren Ali-Ogly, Daniil Nikitin, Pavel Solař, Jiří Kratochvíl, Mykhailo Vaidulych, et al., Particle & Particle Systems Characterization **37**, 1900436 (2020).

[120] Ehsan H Sabbar, Nitun N Poddar, and Jacques G Amar, Physica A: Statistical Mechanics and its Applications **508**, 567 (2018).

[121] TJ Oliveira and FDA Aarao Reis, Physical Review B **83**, 201405 (2011).

[122] R A Puglisi, G Nicotra, S Lombardo, C Spinella, G Ammendola, M Bileci, and C Gerardi, Surf Sci **550**, 119 (2004).

[123] JA Venables and GDT Spiller, *Surface Mobilities on Solid Materials* (Springer, New York, 1983), pp. 341–404.

[124] Cooper J. C. Kimoto T., in *Fundamentals of Silicon Carbide Technology* (John Wiley & Sons, Ltd, IEEE press, 2014), Chap. 2, pp. 11–38.

[125] Cooper J. C. Kimoto T., in *Fundamentals of Silicon Carbide Technology* (John Wiley & Sons, Ltd, IEEE press, 2014), Chap. 10, pp. 417–444.

[126] Fabrizio Roccaforte, Patrick Fiorenza, Giuseppe Greco, Raffaella Lo Nigro, Filippo Giannazzo, Alfonso Patti, and Mario Saggio, physica status solidi (a) **211**, 2063 (2014).

[127] Wolfgang Wondrak, Raban Held, Ekkehard Niemann, and Ulrich Schmid, IEEE Transactions on Industrial Electronics **48**, 307 (2001).

[128] Xu She, Alex Q. Huang, Óscar Lucía, and Burak Ozpineci, IEEE Transactions on Industrial Electronics **64**, 8193 (2017).

[129] Evgeniy N. Mokhov, in *Crystal Growth*, edited by Vadim Glebovsky (IntechOpen, Rijeka, 2018), Chap. 2.

[130] Ulrich M Gosele, Annual Review of Materials Science **18**, 257 (1988).

[131] U M Gosele, Annual Review of Materials Science **18**, 257 (1988).

[132] Y Negoro, T Kimoto, H Matsunami, F Schmid, and G Pensl, Journal of Applied Physics **96**, 4916 (2004).

[133] T Troffer, M Schadt, T Frank, H Itoh, G Pensl, J Heindl, HP Strunk, and M Maier, physica status solidi (a) **162**, 277 (1997).

[134] C Darmody and N Goldsman, Journal of Applied Physics **126**, 145701 (2019).

[135] E Wendler, A Heft, and W Wesch, Nuclear Instruments and Methods in Physics Research Section B: Beam Interactions with Materials and Atoms **141**, 105 (1998).

[136] Man Xu, Yarabahally R Girish, Kadalipura P Rakesh, Piye Wu, Honnayakanahalli M Manukumar, Shayan M Byrappa, Kullaiah Byrappa, et al., Materials Today Communications **28**, 102533 (2021).

[137] Oren Cooper, Hoang-Phuong Phan, Bei Wang, Sean Lowe, Christopher J. Day, Nam-Trung Nguyen, and Joe Tiralongo, Langmuir **36**, 13181 (2020), pMID: 33104368.

[138] M. Auernhammer, S. J. Schoell, M. Sachsenhauser, K.-C. Liao, J. Schwartz, I. D. Sharp, and A. Cattani-Scholz, Applied Physics Letters **100**, 101601 (2012).

[139] Alexandra Oliveros, Sebastian J. Schoell, Christopher Frewin, Marco Hoeb, Martin Stutzmann, Ian D. Sharp, and Stephen E. Saddow, MRS Online Proceedings Library (OPL) **1235**, 1235–RR03 (2009).

[140] Chin-Che Tin, Suwan Mendis, Michelle Tin, and John Williams, Journal of Applied Physics **114**, 244502 (2013).

[141] P Nash and A Nash, Bulletin of Alloy Phase Diagrams **8**, 6 (1987).

Acknowledgements

Innanzitutto vorrei ringraziare la Prof.ssa Maria Grazia Grimaldi per il suo ruolo di supervisore di questo dottorato.

Un grazie va a Rosaria Puglisi, per avermi guidato nel mondo della ricerca e per l'impegno costante nonostante le difficoltà.

Ringrazio l'Istituto per la Microelettronica e Microsistemi del Consiglio Nazionale delle Ricerche (IMM-CNR) e i suoi membri. Un grazie particolare va a Salvatore Pannitteri e Corrado Bongiorno per le lunghe sessioni al TEM, a Salvatore di Franco per la compagnia in laboratorio, a Markus Italia per il lavoro puntuale e ad Antonino La Magna senza il quale non avrei potuto pubblicare. Inoltre Silvia Scalese per il suo occhio allenato a distinguere dettagli infinitesimali al SEM.

Thanks to Neda Rahmani and Jost Adam for the helpful and insightful contributions to the work of this thesis, and for the long and interesting discussions.

Un grazie va a tutti coloro che bazzicavano con me per i corridoi dell'IMM e in particolare agli abitanti dell'Ex-cucina, con cui ci siamo confrontati ogni giorno.

Grazie ai miei nuovi colleghi, che tentano pazientemente di rispondere alle mie mille domande.

Grazie a miei amici, insieme ai quali cresco ogni giorno, e alla mia famiglia che mi ha sostenuto e mi sostiene.

E un grazie speciale a Viviana, che più di tutti riesce ad incoraggiarmi.

Publications

- Pizzone, M.; Grimaldi, M.G.; La Magna, A.; Rahmani, N.; Scalese, S.; Adam, J.; Puglisi, R.A. *Study of the Molecule Adsorption Process during the Molecular Doping.* Nanomaterials **2021**, 11, 1899.
- Pizzone, M.; Grimaldi, M.G.; La Magna, A.; Scalese, S.; Adam, J.; Puglisi, R.A. *Molecule clustering dynamics in the molecular doping process of Si(111) with diethyl-propylphosphonate* Int. J. Mol. Sci. **2023**, 24, 6877.

Conferences

- SMeet Science Sharing Meetings, as a speaker with the talk "The Molecular Doping, an innovative method for conformal doping"
- EMRS Fall 2021, as a speaker with the abstract: "The bonding mechanisms in the molecular doping process: an experimental and numerical approach. Authors : Pizzone, M., A. La Magna, Grimaldi, M.G., Rahmani, N., Scalese, S., Adam, J. and Puglisi, R.A. - *winner of the Graduate Students Awards, Symposium R*;
- School on Nanotechnologies, Nanoinnovation 2021, as an attendee
- SYNERGY 2021 conference, Silesian University of Technology, with a poster contribution;
- PCAM seminar series 2022/2023, as a speaker, with the talk "A liquid solution based approach for silicon doping"